BIO ACCENT

BAOJ Physics

Alfons Penzkofer, et al., BAOJ Physics 2016, 2: 1
2: 006

Research

# Absorption and Emission Spectroscopic Investigation of Thermal Dynamics and Photo-Dynamics of the Rhodopsin Domain of the Rhodopsin-Guanylyl Cyclase from the Aquatic Fungus *Blastocladiella emersonii*

**Alfons Penzkofer[*1], Ulrike Scheib[2], Peter Hegemann[2] and Katja Stehfest[2]**

[1]*Fakultät für Physik, Universität Regensburg, Universitätsstraße 31, D-93053 Regensburg, Germany*

[2] *Institut für Biologie/Experimentelle Biophysik, Humboldt Universität zu Berlin, Invalidenstraße 42, D-10115 Berlin, Germany*

## Abstract

A new class of rhodopsins covalently linked to an enzymatic domain was discovered recently. A member of this class of enzymerhodopsins, the rhodopsin-guanylyl cyclase (RhGC) was identified in the aquatic fungus *Blastocladiella emersonii* (BE). Characterization of RhGC showed that the second-messenger molecule cGMP (cyclic guanylyl monophosphate) is produced upon green light illumination. Here, the rhodopsin domain Rh (BE) of the rhodopsin-guanylyl cyclase RhGC was studied by absorption and emission spectroscopic methods. It was found that fresh thawed Rh (BE) was composed of a mixture of retinal – protein conformations. These retinal conformations are likely all-*trans* protonated retinal Schiff base (Ret_1), 13-*cis* protonated retinal Schiff base with repositioned counter ion (Ret_2), all-*trans* protonated retinal Schiff base with repositioned counter ion (Ret_3), and deprotonated all-*trans* protonated retinal Schiff base (Ret_4). The Rh (BE) thermal denaturing was studied: An apparent protein melting temperature of $\vartheta_m \approx 49$ °C was determined; the apparent protein melting time at room temperature (≈ 21.9 °C) was $t_m \approx 1.45$ h. Thermal retinal conformation restructuring with irreversible conversion likely to deprotonated 13-*cis* retinal Schiff base (Ret_4') was observed. The photo-excitation of all-*trans* protonated retinal Schiff base (Ret_1) caused a primary photo-cycle dynamics involving excited-state picosecond all-*trans* – 13-*cis* isomerization (13-*cis* protonated retinal Schiff base Ret_5 formation) followed by ground-state sub-second intermediate retinal Schiff base formations (Ret_2, Ret_3, Ret_4) and sub-second to second recovery to the initial all-*trans* protonated retinal Schiff base (Ret_1). Long-time all-*trans* protonated retinal Schiff base photo-excitation caused irreversible (likely 13-*cis*) retinal Schiff base (Ret_4') formation.

**Keywords:** Rhodopsin Domain; Rhodopsin-Guanylyl Cyclase; *Blastocladiella emersonii*; Retinal Schiff Base

## 1. Introduction

The unicellular eukaryotic water mold *Blastocladiella emersonii* (common name: aquatic fungus) [1] belongs to the family of *Blastocladiaceae* [2]. Spores of fungi in the family *Blastocladiaceae* are phototactic [3,4] requiring cyclic guanosine monophosphate (cGMP) [5] and rhodopsin [6] for photo-orientation [3,4]. A microbial rhodopsin sequence (type-I rhodopsin) connected to a guanylyl cyclase domain through a 46-amino acid residue linker in *Blastocladiella emersonii* was revealed by genomic sequence analysis [4]. The optogenetic behavior of the rhodopsin-guanylyl cyclase (RhGC) of *Blastocladiella emersonii* was studied in [5,6]. Upon application of a short green light flash, recombinant RhGC converted with a time constant of 8 ms into a signaling state with blue-shifted absorption from which the dark state recovered with a time constant of 93 ms at 22 °C [7]. When expressed in *Xenopus* oocytes [7,8], Chinese hamster ovary cells [7], human embryonic kidney cells [8], rat hippocampal neurons [7], muscle cells and sensory neurons of the nematode *Caenorhabditis elegans* [8], RhGC generated cGMP in response to green light in a light dose-dependent manner on a sub-second time scale.

The rhodopsin-guanylyl cyclase RhGC belongs to the class of enzymerhodopsins a new subfamily of microbial rhodopsins which consist of a rhodopsin domain and an enzyme domain [9-13]. The light activation of the rhodopsin part triggers the action of the enzyme part for biological reaction. Light-gated enzymes belong to the toolkits of optogenetics[14-16].

In this paper the absorption and emission spectroscopic behavior of the thermal dynamics and the photo-dynamics of the rhodopsin domain Rh (BE) of the rhodopsin-guanylyl cyclase RhGC from *Blastocladiella emersonii* is studied in detail. It was found that fresh thawed Rh (BE) is composed of a mixture of retinal – protein conformations. In absorption spectroscopic analysis of protein heating the apparent protein melting temperature of Rh (BE)

***Corresponding author:** Alfons Penzkofer, Fakultät für Physik, Universität Regensburg, Universitätsstraße 31, D-93053 Regensburg, Germany, E-mail: alfons.penzkofer@physik.uni-regensburg.de

**Rec Date:** December 9, 2016, **Acc Date:** December 19, 2016, **Pub Date**: December 19, 2016.

**Citation:** Alfons Penzkofer, Ulrike Scheib, Peter Hegemann and Katja Stehfest (2016) Absorption and Emission Spectroscopic Investigation of Thermal Dynamics and Photo-Dynamics of the Rhodopsin Domain of the Rhodopsin-Guanylyl Cyclase from the Aquatic Fungus *Blastocladiella emersonii*. BAOJ Physics 2: 006.

was determined. The apparent protein melting time of Rh (BE) was determined as a function of sample temperature. The photo-excitation of all-*trans* protonated retinal Schiff base caused a primary photo-cycle dynamics involving picoseconds excited-state all-*trans* – 13-*cis* isomerization, followed by 0.1 second protonated retinal Schiff base intermediate formations and the sub-second to second recovery to the initial all-*trans* protonated retinal Schiff base. Long-time protonated all-*trans* retinal Schiff base photo-excitation caused irreversible 13-*cis* deprotonated retinal Schiff base formation. A primary photo-cycle scheme and a secondary photo-conversion scheme for Rh (BE) is developed. The photo-physical behavior of Rh (BE) is compared with other microbial (type-I) rhodopsins.

## 2. Experimental

### 2.1. Sample Preparation

The recombinant synthesis of the rhodopsin domain Rh (BE) in methylotropic yeast *Pichia pastoris* was reported in the spectroscopic analysis of recombinant proteins section in [7]. Rh (BE) apoprotein consists of 396 amino acids (molar mass $M_{apo}$ = 43 071.2 g mol$^{-1}$). It covalently binds the cofactor retinal. The amino acid sequence is displayed in Fig.S1 of the Supplementary material (section S1). The present 11 Trp (W), 15 Tyr (Y), and 22 Phe (F) are mainly responsible for the UV absorption. The structural formulae of lysine coupled all-*trans* protonated retinal Schiff base $PRSB^+_{trans}$, all-*trans* deprotonated retinal Schiff base $RSB_{trans}$, 13-*cis* protonated retinal Schiff base $PRSB^+_{cis}$, and 13-*cis* deprotonated retinal Schiff base $RSB_{cis}$ are shown in Fig.S2 of the Supplementary material (section S2).

### 2.2. Spectroscopic Investigations

The Rh (BE) protein in pH 8.0 Tris buffer (20 mM tris (hydroxymethyl) aminomethane, 100 mM NaCl, 0.02 % dodecylmaltoside (DDM), 0.1 mM phenylmethylsulfonyl fluoride (PMSF)) was stored at -80 °C. Before usage it was thawed and kept in the dark at about 4 °C. Absorption, fluorescence, short-time photo-cycle, and long-time photo-conversion measurements were carried out at room temperature, if not stated differently. The Rh (BE) solutions were investigated in fused silica ultra-micro cells from Hellma Analytics, Müllheim, Germany (for absorption measurements cell inner size 1.5×3×5 mm$^3$, for fluorescence measurements cell inner size 2×10×5 mm$^3$).

Transmission measurements, $T(\lambda)$, were carried out with a spectrophotometer (Cary 50 from Varian). Attenuation coefficient spectra were calculated by the relation, $\alpha(\lambda) = -\ln[T(\lambda)]/l$, where $l$ is the sample length. The attenuation coefficient α is composed of absorption, $\alpha_a$, and scattering, $\alpha_s$, contributions according to $\alpha(\lambda)=\alpha_a(\lambda)+\alpha_s(\lambda)$. In the transparency region only scattering attenuates the light in the sample passage. $\alpha_s(\lambda)$ is approximated by the empirical relation [17] $\alpha_s(\lambda) = \alpha(\lambda_0)(\lambda_0/\lambda)^\gamma$ where $\lambda_0$ is selected in the transparency region and $\gamma \le 4$ is fitted to the experimental attenuation in the transparency region ($\gamma = 4$ for small particles in the Rayleigh scattering regime, and $\gamma < 4$ for larger particle size in the Mie scattering regime). Absorption coefficient spectra $\alpha_a(\lambda)$ became available by subtracting the scattering contribution $\alpha_s(\lambda)$ from the measured attenuation spectra $\alpha(\lambda)$.

For fluorescence spectroscopic measurements a spectrofluorimeter (Cary Eclipse from Varian) was used (cell length in excitation direction 1 cm, cell width in detection direction 2 mm). Fluorescence quantum distributions $E_F(\lambda)$ were determined from fluorescence emission spectrum measurements at fixed excitation wavelengths [18-20]. The dye rhodamine 6G in methanol (fluorescence quantum yield $\phi_{F,ref}$ = 0.94 [21]) was used as reference standard for fluorescence quantum distribution calibration. The fluorescence quantum yield is given by $\phi_F = \int_{em} E_F(\lambda) d\lambda$ where the integration runs over the fluorescence emission wavelength region. The fluorescence spectra were deprived from scattering contributions by separate spectra measurements using a water solution of Ludox CL-X colloidal silica from DuPont with particle size of 21 nm diameter and appropriate scattering contribution subtraction.

For absorption spectroscopic photo-cycling and photo-conversion investigations, Rh (BE) samples were excited with a cw frequency doubled Nd:YAG laser (wavelength $\lambda_{exc}$ = 532 nm). The sample solution in a 1.5×3×5 mm$^3$ fused silica ultra-micro cell in the Cary 50 spectrophotometer for transmission measurements was irradiated with the laser transverse to the transmission detection path (exposed area 3×5 mm$^2$, sample thickness along excitation path 1.5 mm, transmission detection path 3 mm). The excitation power $P_{exc}$ was measured with a power meter (model PD 300-UV-SH photodiode detector head with NOVA power monitor from Ophir). The excitation intensity $I_{exc}$ was calculated by the relation $I_{exc} = P_{exc} / A_{cell}$ with cell area $A_{cell}$ = 0.15 cm$^2$.

The thermal protein stability of Rh (BE) was investigated by apparent protein melting temperature and temperature dependent apparent melting time determination [22]. The apparent protein melting temperature of Rh (BE) was determined by stepwise sample heating up and then cooling down, whereby transmission spectra were measured and the rising light scattering with sample heating was analyzed [22]. The apparent protein melting times at fixed temperatures were determined by storing Rh (BE) samples at selected temperatures in the dark and measuring transmission spectra at certain time intervals whereby the temporal light scattering development was analyzed [22].

## 3. Results

### 3.1. Sample Absorption and Emission Behavior of Freshly Thawed Rh (BE)

#### 3.1.1. Absorption Behavior

The attenuation coefficient spectrum $\alpha(\lambda)$ of a fresh Rh (BE) sample measured immediately after thawing and centrifugation at 4400 rpm for 15 min at 4 °C is displayed by the solid curve in Fig.1. The dotted curve shows the light scattering contribution $\alpha_s(\lambda)$ fitted by $\alpha_s(\lambda) = \alpha(\lambda_0)(\lambda_0/\lambda)^\gamma$ with $\lambda_0$ = 800 nm, $\alpha(\lambda_0)$ = 0.02 cm$^{-1}$ and $\gamma$ = 4. This scattering strength agrees with a mean Rh (BE) aggregation size of $\beta_m \approx$ 790 monomers per Rh (BE) cluster as analyzed in the Supplementary material section S3. The dashed curve shows the absorption coefficient contribution $\alpha_a(\lambda)=\alpha(\lambda)-\alpha_s(\lambda)$ of Rh (BE).

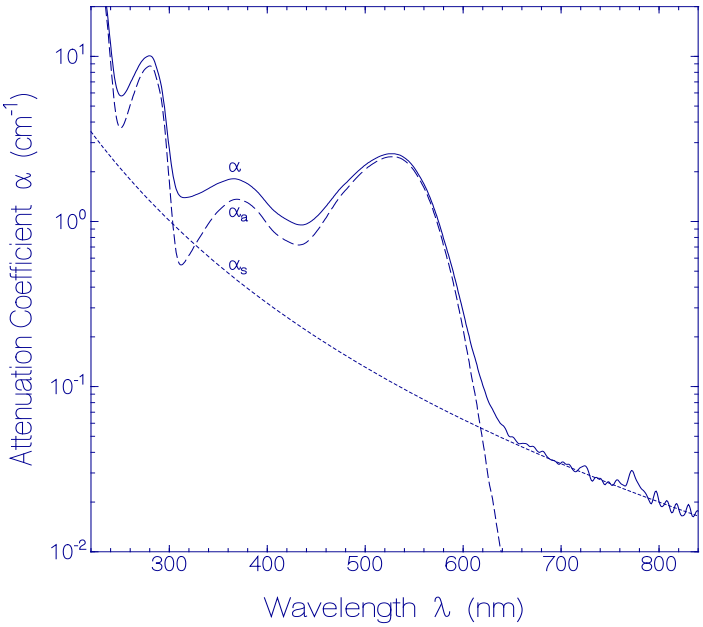


**Fig.1:** Attenuation coefficient spectrum of a fresh Rh (BE) sample in pH 8 Tris buffer. Solid curve: attenuation coefficient spectrum α(λ) measured after sample centrifugation (4400 rpm for 15 min at 4°C). Dotted curve: approximate scattering contribution $\alpha_s(\lambda)$ calculated by using $\alpha_s(\lambda) = \alpha(\lambda_0)(\lambda_0/\lambda)^\gamma$ with $\lambda_0$ = 800 nm, $\alpha(\lambda_0)$ = 0.02 cm$^{-1}$ and γ = 4. Dashed curve: approximate absorption coefficient spectrum $\alpha_a(\lambda) = \alpha(\lambda) - \alpha_s(\lambda)$.

The absorption coefficient spectrum of Rh (BE) is composed of the retinal absorption in the wavelength region of λ > 330 nm, and the combined apoprotein and retinal absorption in the wavelength region λ < 330 nm (see section S4 of the Supplementary material).

### 3.1.2. Fluorescence Behavior

In order to gain information on possibly existing retinal – protein conformations in Rh (BE) fluorescence spectra were measured on another fresh centrifuged Rh (BE) sample using fluorescence excitation wavelengths extending over the absorption spectrum region. The obtained fluorescence emission quantum distributions $E_F(\lambda)$ of fresh Rh (BE) at excitation wavelengths in the region from $\lambda_{F,exc}$ = 530 nm to 270 nm are displayed in Fig.2. The corresponding fluorescence quantum yield curve is shown in Fig.3.

The variation of the fluorescence quantum distribution with the fluorescence excitation wavelength indicates multi-component fluorescence emission from different species (for a single component an excitation-wavelength-independent $S_1 \rightarrow S_0$ emission of constant shape and quantum yield is expected [23,24]). The fluorescence emissions of the species with decreasing fluorescence excitation wavelength are mixed up i) because the absorption bands of the different species overlap and ii) because the species are in Rh (BE) clusters (aggregates, short distance between donor and acceptor) with efficient Förster-type energy transfer [18] from short-wavelength emitting species (donors) to long-wavelength emitting species (acceptors) [18,25].

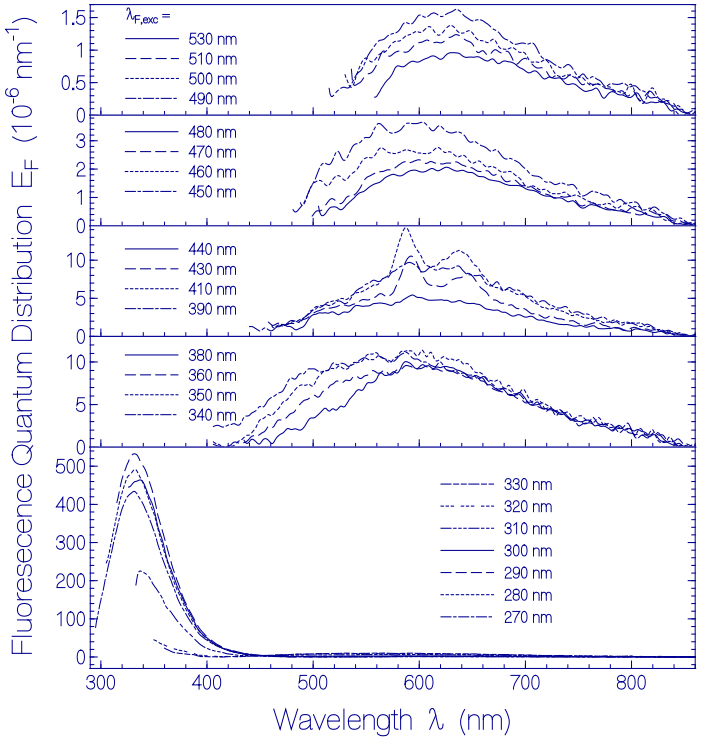


**Fig.2:** Fluorescence emission quantum distributions $E_F(\lambda)$ of fresh Rh (BE) for various fluorescence excitation wavelengths $\lambda_{F,exc}$ in the region from 530 nm to 270 nm.

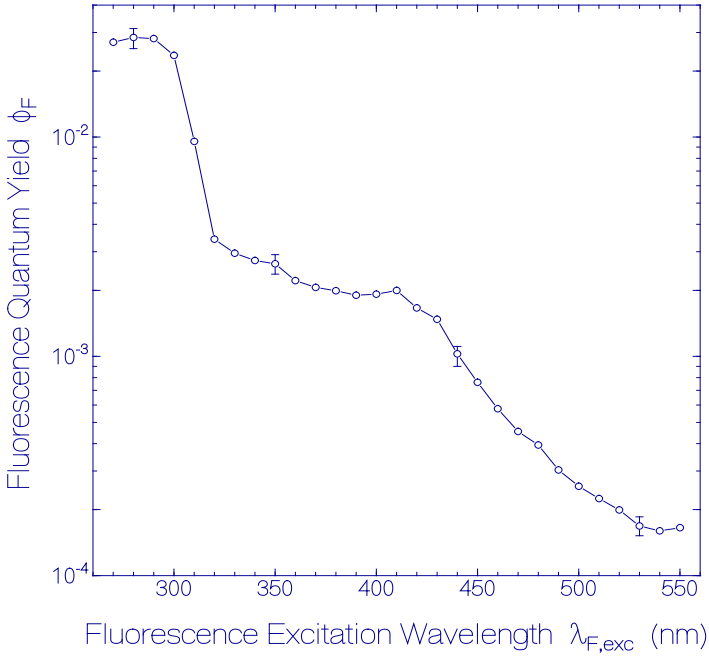


**Fig.3:** Dependence of fluorescence quantum yield ϕ of fresh Rh (BE) versus fluorescence excitation wavelength $\lambda_{F,exc}$ in the region from 550 nm to 270 nm.

The fluorescence quantum distributions presented in the sub-sets of Fig.2 indicate the emission of different emitting retinal conformations in the rhodopsin protein (Ret_1, Ret_2, Ret_3,

Ret_4) and the apoprotein emission.

Ret_1 causes the main Rh (BE) absorption band around 530 nm. It is likely protonated all-*trans* retinal Schiff base $PRSB^{+}_{trans}$ [7,11]. Its fluorescence quantum yield is $\phi_{F,Ret\_1} \approx \phi_F(530\ nm) = (1.7\pm0.3) \times 10^{-4}$.

The absorption spectrum contribution of Ret_2 is hidden below the first broad absorption band peaking around 530 nm. It is likely protonated 13-*cis* retinal Schiff base with repositioned counter ion $PRSB^{+}_{cis,cirp}$(see below). Its first absorption peak is at $\lambda_{A,Ret\_2} \approx 440$ nm (see Fig.S3). Its absorption contribution $\kappa_{abs,Ret\_2} = \alpha_{a,Ret\_2}(\lambda_{A,Ret\_2})/\ \alpha_a(\lambda_{A,Ret\_2})$ is estimated to be $\kappa_{abs,Ret\_2} \approx 0.5$. The fluorescence quantum yield of Ret_2 is $\phi_{F,Ret\_2} \approx \phi_F(440\ nm)/\ k_{abs,Ret\_2} = (2\pm0.2) \times 10^{-3}$. The fluorescence emission of Ret_2 is quenched by Förster-type energy transfer [13,18] from Ret_2 to Ret_1 within the Rh (BE) aggregates with small Ret_1 emission (emission band of Ret_2 overlaps with absorption band of Ret_1).

Ret_3 contributes to the absorption around 415 nm (see Fig.S3). It is likely protonated all-*trans* retinal Schiff base with repositioned counter ion $PRSB^{+}_{trans,cirp}$(see below). Its absorption contribution is estimated to be $\kappa_{abs,Ret\_3} \approx 0.5$. The fluorescence quantum yield of Ret_3 is $\phi_{F,Ret\_3} \approx \phi_F(415\ nm)/\ \kappa_{abs,Ret\_3} = (4\pm0.4) \times 10^{-4}$. The fluorescence spectrum of Ret_3 includes a well resolved vibronic structure with peaks at 587 nm and 638 nm (vibronic wavenumber spacing $\delta\tilde{\nu} \approx 1360\ cm^{-1}$). The fluorescence emission of Ret_3 is quenched by Förster-type energy transfer from Ret_3 to Ret_1 within the Rh (BE) aggregates with small Ret_1 emission (emission band of Ret_3 overlaps with absorption band of Ret_1). Förster-type energy transfer from Ret_3 to Ret_2 is thought to be less efficient because the emission band of Ret_3 has only weak overlap with the absorption band of Ret_2.

Ret_4 contributes to the absorption around 360 nm (see Fig. S3). It is likely deprotonated all-*trans* retinal Schiff base $RSB_{trans}$ (see below) [7,11,13]. Its absorption contribution is estimated to be $k_{abs,Ret\_4} \approx 0.8$. The fluorescence quantum yield of Ret_4 is $\int_{405\ nm}^{540\ nm} E_{F,\lambda_F,exc=360\ nm}(\lambda)d\lambda\ /\kappa_{abs,Ret\_4} = (6.3\pm1) \times 10^{-4}$. The fluorescence emission of Ret_4 is thought to be partly quenched by Förster-type energy transfer from Ret_4 to Ret_1 within the Rh (BE) aggregates with small Ret_1 emission (emission band of Ret_4 in the region from 400 nm to 540 nm partly overlaps with absorption band of Ret_1). The shape of the fluorescence spectrum of Ret_4 for $\lambda > 540$ nm is determined by efficient Ret_4 to Ret_3 and Ret_2 Förster-type energy transfer.

The fluorescence quantum distributions shown in the bottom part of Fig.2 are dominantly caused by apoprotein and apoprotein tail excitation. The apoprotein fluorescence is attributed to Trp emission with typical fluorescence emission maximum around 330 nm. The maximum absorption position of Trp is $\lambda_{A,Trp} \approx 280$ nm. The absorption contribution is $\kappa_{abs,Apo} \approx 0.87$ (see Fig.S3). Tyr emission with typical emission maximum around 308 nm is not observed because of efficient Tyr to Trp Förster-type energy transfer within the apoprotein (see supplementary material to [13]). The fluorescence quantum yield of apoprotein is $\phi_{F,Apo} \approx \phi_F(280\ nm)/\ \kappa_{abs,Apo} = 0.033\pm0.004$. The fluorescence emission of the apoprotein is thought to be partly quenched by Förster-type energy transfer from Apo to Ret_1, Ret_2, Ret_3, and Ret_4 within the Rh (BE) aggregates. The small emission for $\lambda > 450$ nm is due to emission from Ret_2, Ret_3 and Ret_4 after Förster-type energy transfer.

The fluorescence lifetimes (lifetimes of emitting states) of the considered species *i* are determined by the fluorescence quantum yields $\phi_{F,i}$ and the radiative lifetimes $\tau_{rad,i}$ according to

$$\tau_{F,i} = \phi_{F,i}\tau_{rad,i} \tag{1}$$

The radiative lifetimes of the transitions are given by the Strickler-Berg relation [26-28]

$$\tau_{rad,i} = \frac{n_A \bar{\lambda}_{F,i}^3}{8\pi c_0 n_F^3 \bar{\sigma}_i} \tag{2}$$

where $n_A$ and $n_F$ are the mean refractive indices in the first absorption band region and the fluorescence region of the considered species, respectively (determined by the water solvent), $\bar{\lambda}_{F,i} = \left[\int E_{F,i}(\lambda)\lambda^3 d\lambda / \int E_{F,i}(\lambda)d\lambda\right]^{1/3}$ are the mean fluorescence wavelengths, and $\bar{\sigma}_i = \int_{1st\ band}[\sigma_i(\lambda)/\lambda]d\lambda$ are the $S_0$-$S_1$ absorption band cross-section strengths of the $S_0$-$S_1$ transitions.

In Table 1 – besides other parameters - approximate and estimated values of peak absorption wavelengths $\lambda_{A,i}$, mean fluorescence wavelengths $\bar{\lambda}_{F,i}$, mean refractive indices $n_{A,i}$ and $n_{F,i}$, absorption contributions $\kappa_{abs,i}$, fluorescence quantum yields $\phi_{F,i}$, $S_0$-$S_1$absorption band cross-section strengths $\bar{\sigma}_i$, radiative lifetimes $\tau_{rad,i}$, and Strickler-Berg based fluorescence lifetimes $\tau_{F,i}$ of the species *i* are collected. The $S_0$-$S_1$ absorption band cross-section strength $\bar{\sigma}_{Ret\_1}$ of the retinal species Ret_1 is $\bar{\sigma}_{Ret\_1} = (3.3\pm0.3)\times10^{-17}\ cm^{-2}$. It was determined from Fig.S3 using $\bar{\sigma}_{Ret\_1} = \int_{\lambda \geq 440\ nm}\left[\sigma_{Ret\_1}(\lambda)/\lambda\right]d\lambda = \int_{\lambda \geq 440\ nm}\left[\sigma(\lambda)/(\kappa_{Ret\_1}\lambda)\right]d\lambda$ with $\kappa_{Ret\_1} \approx 0.57$ (see Eq.3 below). The $S_0$-$S_1$ absorption band cross-section strengths of Ret_2, Ret_3, and Ret_4 are thought to be roughly the same as the $S_0$-$S_1$ absorption band cross-section strength of Ret_1 [13]. In the calculation of $\kappa_{rad,i}$ (Eq.2) they are set equal to the value of Ret_1. The value of $\bar{\sigma}_{Apo}$ was determined using the absorption cross-section spectrum of Trp, i.e. $\bar{\sigma}_{Apo} = \bar{\sigma}_{Trp} = \int_{\lambda \geq 240\ nm}[\sigma_{Trp}(\lambda)/\lambda]d\lambda$ (from [29], incoherent independent emission of each Trp residue in the protein).

**Table 1:** Spectroscopic parameters of retinals and apoprotein in fresh thawed Rh (BE).

| Parameter | Ret_1 | Ret_2 | Ret_3 | Ret_4 | Apo |
|---|---|---|---|---|---|
| $\lambda_A$ (nm) | 530 | 440 | 415 | 360 | 280 |
| $n_A$ | 1.335 | 1.340 | 1.342 | 1.35 | 1.365 |
| $\bar{\lambda}_F$ (nm) | 673 | 580.7 | 606.5 | 457.4 | 344.9 |
| $n_F$ | 1.330 | 1.333 | 1.333 | 1.338 | 1.350 |
| $\alpha_a(\lambda_A)$ (cm$^{-1}$) | 2.46 | 0.748 | 0.791 | 1.31 | 8.74 |
| $\kappa_{abs}$ | 1 | ≈ 0.5 | ≈ 0.5 | ≈ 0.8 | ≈ 0.87 |
| $\alpha_{a,Ret\_i}(\lambda_A)$ (cm$^{-1}$) | 2.46 | ≈ 0.374 | ≈ 0.396 | ≈ 1.05 | |
| $\kappa_{Ret\_i}$ | ≈ 0.57 | ≈ 0.087 | ≈ 0.093 | ≈ 0.25 | |
| $\tilde{\nu}_{i,1}$ (cm$^{-1}$) | 0 | 384 | 373 | 174 | |
| $\phi_{F,i}$ | (1.7±0.3)×10$^{-4}$ | (2±0.2)×10$^{-3}$ | (4±0.4)×10$^{-3}$ | (6.3±1)×10$^{-4}$ | 0.033±0.004 |
| $\bar{\sigma}$ (cm$^2$) | (3.3±0.3)×10$^{-17}$ | ≈ 3.3×10$^{-17}$ | ≈ 3.3×10$^{-17}$ | ≈ 3.3×10$^{-17}$ | (3.0±0.1)×10$^{-18}$ |
| $\tau_{rad}$ (ns) | ≈ 6.95 | ≈ 4.45 | ≈ 5.0 | ≈ 2.2 | ≈ 10.1 |
| $\tau_F$ (ps) | ≈ 1.2 | ≈ 8.9 | ≈ 20 | ≈ 1.4 | ≈ 410 |

Abbreviations: $\lambda_A$: peak $S_0$-$S_1$ absorption wavelength. $n_A$: mean refractive index in $S_0$-$S_1$ absorption region. $\bar{\lambda}_F$ : mean $S_1$-$S_0$ fluorescence wavelength. $n_F$: mean refractive index in $S_1$-$S_0$ fluorescence region. $\alpha_a(\lambda_A)$: absorption coefficient at wavelength $\lambda_A$. $\kappa_{abs}$: absorption contribution of considered species at $\lambda_A$. $\alpha_{a,Ret\_i}(\lambda_A)$: absorption coefficient of species Ret_i at wavelength $\lambda_A$. $\kappa_{Ret\_i}$: fraction of retinal species *i*. $\tilde{\nu}_{i,1}$ : ground-state energy difference between species Ret_i and Ret_1 in wavenumbers. $\phi_{F,i}$: fluorescence quantum yield of species *i*. $\bar{\sigma}$ : $S_0$-$S_1$ absorption band cross-section strength of species *i*. $\tau_{rad}$: radiative lifetime of species *i*. $\tau_F$: fluorescence lifetime of species *i*.

For Ret_1 (likely protonated all-*trans* retinal Schiff base $PRSB^+_{trans}$) the fluorescence quantum yield is $\phi_{F,Ret\_1}$ = (1.7±0.3)×10$^{-4}$. The radiative lifetime is $\tau_{rad,Ret\_1}$ ≈ 6.95 ns and the fluorescence lifetime is $\tau_{F,Ret\_1}$ = 1.2±0.3 ps. This short fluorescence lifetime fits with barrier-less first excited state twist to a funnel position (conical intersection position [30]) where fast internal conversion from the excited state $S_1$ potential energy surface to the $S_0$ ground-state potential energy surface occurs (twisted internal conversion [31]) with partial transfer to a product (photo-isomer) and partial recovery to the initial educt conformation [13,30].

For Ret_2 (likely protonated 13-*cis* retinal Schiff base with repositioned counter ion $PRSB^+_{cis,cirp}$) the fluorescence quantum yield is $\phi_{F,Ret\_2}$ = (2±0.2)×10$^{-3}$. The radiative lifetime is $\tau_{rad,Ret\_2}$ ≈ 4.45 ns and the fluorescence lifetime is $\tau_{F,Ret\_2}$ = 8.9±1 ps. It is about a factor of 7.4 larger than the fluorescence lifetime of Ret_1. This lifetime is shortened by Förster-type energy transfer from Ret_2 to Ret_1 within the Rh (BE) aggregates. The true intrinsic Ret_2 fluorescence lifetime $\tau_{F,0,Ret\_2}$ may be in the hundred ps region. There seems to be a barrier between the locally excited $S_1$ state position of Ret_2 and the funnel $S_1$ state position of Ret_2 caused by the retinal surrounding amino acid conformation.

For Ret_3 (likely protonated all-*trans* retinal Schiff base with repositioned counter ion $PRSB^+_{trans,cirp}$) the fluorescence quantum yield is $\phi_{F,Ret\_3}$ = (4±0.4)×10$^{-3}$. The radiative lifetime is $\tau_{rad,Ret\_3}$ ≈ 5.03 ns and the fluorescence lifetime is $\tau_{F,Ret\_3}$ = 20±2 ps. It is shortened by Förster-type energy transfer from Ret_3 to Ret_1 within the Rh (BE) aggregates. The true intrinsic Ret_3 fluorescence lifetime $\tau_{F,0,Ret\_3}$ may be in the hundred ps region indicating a barrier between the locally excited-state $S_1$ position of Ret_3 and the funnel $S_1$ state position of Ret_3.

For Ret_4 (likely deprotonated retinal Schiff base RSB in all-*trans* conformation) the fluorescence quantum yield is $\phi_{F,Ret\_4}$ = (6.3±1) ×10$^{-4}$, the radiative lifetime is $\tau_{rad,Ret\_4}$ ≈ 2.17 ns, and fluorescence lifetime is $\tau_{F,Ret\_4}$ = 1.4±0.2 ps. This short fluorescence lifetime is due to efficient Förster-type energy transfer from Ret_4 to Ret_3, Ret_2, and Ret_1.

The apoprotein behavior is determined by Trp emission. Its fluorescence quantum yield is $\phi_{F,Apo}$≈ 0.033, its radiative lifetime is $\tau_{rad,Apo}$ ≈ 10.1 ns, and its fluorescence lifetime $\tau_{F,Apo}$ ≈ 410 ps. The apoprotein fluorescence emission is quenched by Förster-type energy transfer from apoprotein to retinal. The fluorescence quantum yield of Trp outside the protein in aqueous solution is $\phi_F$ = 0.13 [32-34].

### 3.1.3. Ground-State Retinal Conformations of Rh (BE)

A fresh thawed Rh (BE) sample contained several retinal species (see Fig.S3).

The approximate mole-fractions $\kappa_{Ret\_i}$ of retinal species *i* of a fresh thawed sample are derived from the corresponding absorption fractions $\kappa_{abs,i}$ assuming equal absorption strengths of the various retinal species. Then it is

$$\kappa_{Ret\_i} = \frac{\alpha_{Ret\_i}(\lambda_{A,Ret\_i})}{\sum_j \alpha_{Ret\_j}(\lambda_{A,Ret\_j})} = \frac{\kappa_{abs,Ret\_i}\alpha(\lambda_{A,Ret\_i})}{\sum_j \kappa_{abs,Ret\_j}\alpha(\lambda_{A,Ret\_j})} \quad (3)$$

The obtained approximate mole-fractions from Fig.1 and Fig.S3 are $\kappa_{Ret\_1}$ ≈ 0.57, $\kappa_{Ret\_2}$ ≈ 0.087, $\kappa_{Ret\_3}$ ≈ 0.093, and $\kappa_{Ret\_4}$ ≈ 0.25. (see Table 1).

The ground-state energy level positions $E_{j,1}$ (j = 2,3,4) relative to

Ret_1 are obtained from the thermal equilibrium relation [35]

$$\frac{\kappa_{\mathrm{Ret}\_j}}{\kappa_{\mathrm{Ret}\_1}} = \exp\left(-\frac{E_{j,1}}{k_B \vartheta}\right) \tag{4}$$

giving

$$E_{j,1} = hc_0\tilde{\nu}_{j,1} = -k_B\vartheta \ln\left(\frac{\kappa_{\mathrm{Ret\_j}}}{\kappa_{\mathrm{Ret\_1}}}\right). \tag{5}$$

The obtained energy level positions relative to Ret_1 are (temperature $\vartheta$ = 273.15 K+21 K) $E_{2,1} = 7.63\times10^{-21}$ J ($\tilde{\nu}_{2,1}$ = 384 cm$^{-1}$), $E_{3,1} = 7.41\times10^{-21}$ J ($\tilde{\nu}_{3,1}$ = 373 cm$^{-1}$), and $E_{4,1} = 3.46\times10^{-21}$ J ($\tilde{\nu}_{4,1}$ = 174 cm$^{-1}$). The energy level positions are depicted in the inset of Fig.S3.

### 3.2. Temperature Dependent Rh (BE) Development

The Rh (BE) apparent melting temperature and the temperature dependent apparent protein melting time were determined [22]. Protein melting is synonymous to protein denaturation [36]. The temporal retinal chromophore – opsin protein conformation development along with the protein denaturing was investigated. For this purpose the temporal absorption development of Rh (BE) in pH 8 Tris buffer was studied at the temperatures $\vartheta$ = 1.65±0.3 °C and $\vartheta$ = 21.9±0.3 °C.

#### 3.2.1. Apparent Rh (BE) Melting Temperature Determination

In order to get information on the Rh (BE) protein melting temperature a Rh (BE) sample was stepwise heated up from room temperature to 59.9 °C, cooled down, and centrifuged (4400 rpm, 15 min, 4 °C). At the temperature steps attenuation coefficient spectra were measured (see section S5 of the Supplementary material). The apparent Rh (BE) melting temperature $\vartheta_m$ was determined from the position of steep onset of light scattering in the transparency region of the protein (see left inset in Fig.S4a). A value of $\vartheta_m$ = 48.8±2 °C was determined.

#### 3.2.2. Temporal Absorption Development at 1.65 °C

The temporal absorption coefficient development of Rh (BE) at $\vartheta$ = 1.65±0.3 °C is displayed in Fig.4a. Absorption coefficient spectra in the storage time range from $t$ = 0 to 480 h are shown. The absorption of the 530 nm band decreases (Ret_1) and the absorption of the 370 nm band (Ret_4) increases with time. At λ = 435 nm the absorption is nearly time independent.

The inset in Fig.4a shows the temporal absorption coefficient development $\alpha_a(\lambda_{pr})$ at $\lambda_{pr}$= 529 nm (peak Ret_1 absorption), $\lambda_{pr}$= 368 nm (peak Ret_4 absorption), and $\lambda_{pr}$= 435 nm (Ret_2 absorption with Ret_1, Ret_3 and Ret_4 contribution). During the first three days the absorption decrease at 529 nm is smaller than the absorption increase at 368 nm due to additional conversion of Ret_2 and Ret_3 to Ret_4. Then the absorption at 529 nm continues to decrease while the absorption around 368 nm increases only weakly. This behavior may be due to further Ret_1 to Ret_4 conversion overlapping with Rh (BE) sedimentation which decreases the integrated absorption strength in the supernatant. It

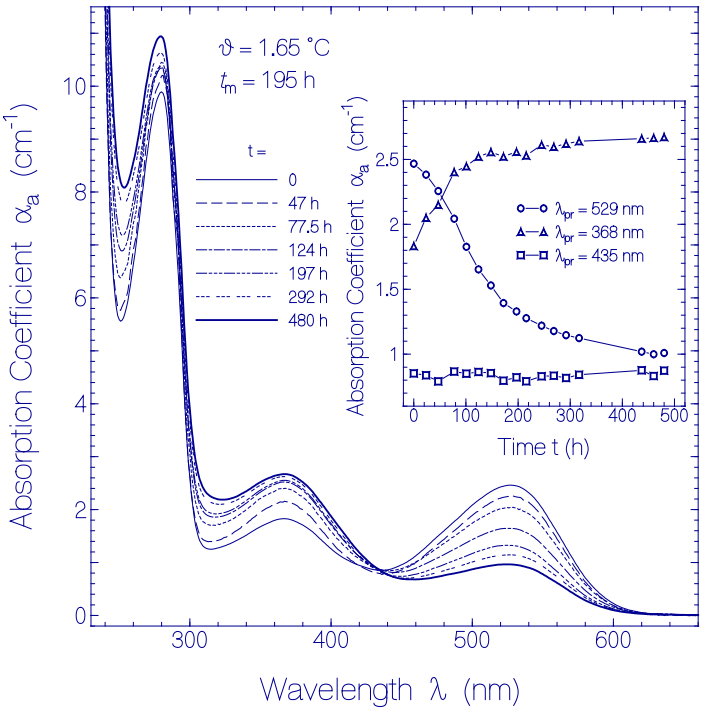


**Fig.4a:** Temporal absorption coefficient spectra development of Rh (BE) at 1.65 °C. Main part: absorption coefficient spectra after various storage times $t$ are shown. The inset shows the absorption coefficient development versus time for the wavelengths $\lambda_{pr}$ = 529 nm (circles), $\lambda_{pr}$ = 368 nm (triangles), and $\lambda_{pr}$ = 435 nm (squares).

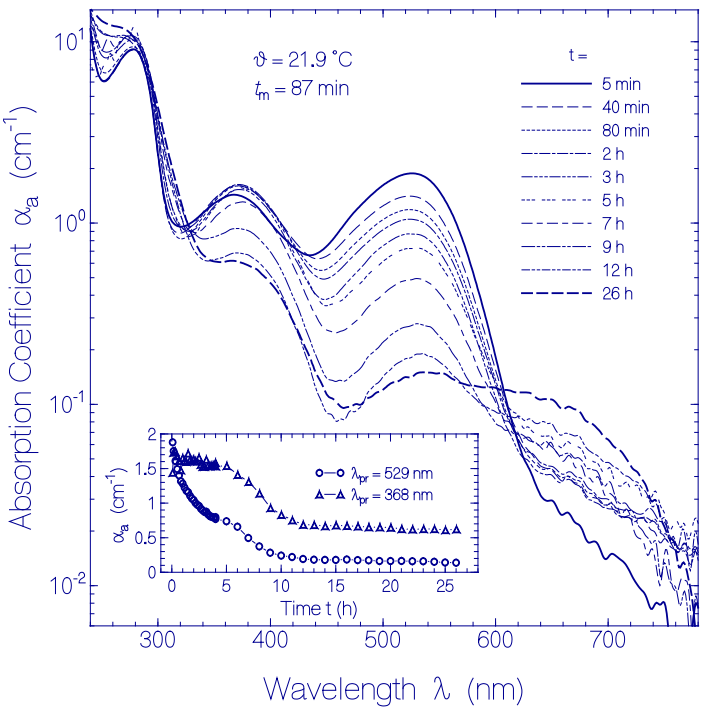


**Fig.4b:** Temporal absorption coefficient spectra development of Rh (BE) at 21.9 °C. Main part: absorption coefficient spectra after various storage times $t$ are shown. The inset shows the absorption coefficient development versus time for wavelengths $\lambda_{pr}$ = 529 nm (circles) and $\lambda_{pr}$ = 368 nm (triangles).

should be noted that the apparent protein melting time is $t_m$(1.65 °C) ≈ 195 h (see Supplementary material section S6), i.e. the retinal species conversion and restructuring occurs concurrent with the protein denaturing.

### 3.2.3. Temporal Absorption Development at 21.9 °C

The temporal absorption coefficient development of Rh (BE) at $\vartheta$ = 21.9±0.3 °C is displayed in Fig.4b. Absorption coefficient spectra in the storage time range from $t$ ≈ 5 min to 26 h are shown. Initially the absorption of the 530 nm band decreased (Ret_1) and the absorption of the 370 nm band (Ret_4) increased with time. After 3 h, the absorption coefficient spectra decreased for λ > 330 nm because of Rh (BE) aggregate sedimentation decreasing the Rh (BE) amount in the supernatant. In the long-wavelength region, λ > 620 nm, absorption was building up with time peaking at ≈ 670 nm indicating some thermal conversion of Ret_1 to a further retinal species Ret_5 along with the protein denaturing. Ret_5 is likely 13-*cis* protonated retinal Schiff base $PRSB^+_{cis}$, see below). It should be noted that the apparent Rh (BE) melting time at $\vartheta$ = 21.9 °C is about 1.45 h (see section S6 of the Supplementary material). In fluorescence emission studies of the Rh (BE) sample after 26 h of storage at 21.9 °C (data not shown) no fluorescence spectrum could be resolved above the noise level for Ret_5 excitation (fluorescence excitation wavelength $\lambda_{F,exc}$ = 680 nm) indicating short fluorescence lifetime and fast photo-isomerization for this retinal species (photo-excitation of Ret_5 is thought to cause excited-state 13-*cis* → all-*trans* isomerization to Ret_1 as does photo-excitation of Ret_1 cause excited-state all-*trans* → 13-*cis* isomerization to Ret_5, see below and Fig.10b).

The inset in Fig.4b shows the absorption coefficient development with time at $\lambda_{pr}$= 529 nm (absorption peak of Ret_1) and $\lambda_{pr}$= 368 nm (absorption peak of Ret_4). In the time range of $t$ < 1.5 h $\alpha_a$(529 nm) decreased and $\alpha_a$(368 nm) increased. In the time range from 1.5 h to 5 h $\alpha_a$(529 nm) decreased and $\alpha_a$(368 nm) was approximately constant due to Ret_1 to Ret_4 conversion and concurrent Rh (BE) sedimentation. In the time range from 5 h to 12 h the absorption coefficients decreased with time due to Rh (BE) aggregate sedimentation giving decreasing Rh (BE) concentration in the supernatant. In the time range from 12 h to 26 h the absorption constants retained nearly constant (no further Rh (BE) sedimentation in the supernatant).

### 3.2.4. Thermal Ground-State Retinal Conformation Restructuring of Rh (BE)

In the stepwise Rh (BE) sample heating for apparent protein melting temperature determination and in the temperature dependent protein melting time determination changes in the retinal species composition were observed (some changes of absorption positions, different amounts of the various species). In Fig.S4b and Table S1 the approximate wavelength positions and approximate amounts of the retinal species in denatured Rh (BE) are presented. Ret_1 is no longer the lowest energetic species. This role is taken over by deprotonated retinal Schiff base which may have changed its conformation from all-*trans* deprotonated retinal Schiff base (Ret_4) to 13-*cis* deprotonated retinal Schiff base (Ret_4') in the denatured protein. Ret_3 seems to be energetically slightly below Ret_1. The ground-state energy level of Ret_2 retains above Ret_1. Ret_5 (likely 13-*cis* protonated retinal Schiff base) in denatured Rh (BE) is energetically lower than in fresh thawed Rh (BE) (there the amount of Ret_5 could not be resolved in the long-wavelength absorption tail of Ret_1 indicating a high-energetic position), but remains the energetically highest lying species.

The estimated mole-fractions $\kappa_{Ret\_i}$(Eq. 3) of retinal species in denatured Rh (BE) are listed in Table S1. They are $\kappa_{Ret\_1}$ ≈ 0.045, $\kappa_{Ret\_2}$ ≈ 0.022, $\kappa_{Ret\_3}$ ≈ 0.063, $\kappa_{Ret\_4}$ ≈ 0.858, and $\kappa_{Ret\_5}$ ≈ 0.012.

The estimated ground-state energy level positions $E_{j,1}$ (j = 2,3,4,5) relative to Ret_1 (Eq.5 with $\vartheta$ = 273.15 K +21 K) are $E_{2,1}$ = -2.91×10$^{-21}$ J ($\tilde{\nu}_{2,1}$ = 146 cm$^{-1}$), $E_{3,1}$ = 1.37×10$^{-21}$ J ($\tilde{\nu}_{3,1}$ = -68.7 cm$^{-1}$), $E_{4,1}$ = 1.2×10$^{-20}$ J ($\tilde{\nu}_{4,1}$ = -602 cm$^{-1}$), and $E_{5,1}$ = 5.37×10$^{-21}$ J ($\tilde{\nu}_{5,1}$ = 270 cm$^{-1}$). The energy level positions are depicted in the inset of Fig.S4b.

### 3.3. Photo-Excitation and Dark Recovery Absorption Dynamics of Rh (BE)

Two fresh thawed Rh (BE) samples were studied for investigation of the photo-cycle dynamics. Both samples were exposed at $\lambda_{exc}$= 532 nm (spatial expanded beam of the second harmonic of a cw Nd:YAG laser). The experiments were carried out at room

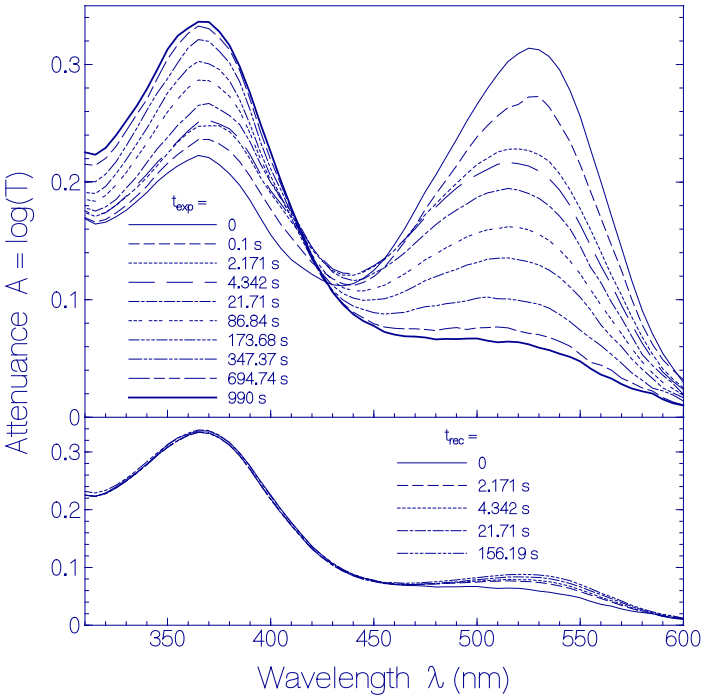


**Fig.5:** Photo-excitation and dark-recovery behavior of Rh (BE) sample due to cw laser exposure at 532 nm using intensity $I_{exc}$ ≈ 16 mW cm$^{-2}$. Temperature $\vartheta$ = 21.2±0.2 °C. Sample size: 3×5×1.5 mm$^3$. Exposure perpendicular to 3×5 mm$^2$ surface (excitation path length 1.5 mm). Length of attenuance probing cell was 3 mm. The top part shows attenuance spectra for various times $t_{exp}$ of sample exposure. The bottom part shows attenuance spectra for various times $t_{rec}$ after excitation light switch-off. Excitation was switched off at $t_{exp}$ = 990 s.

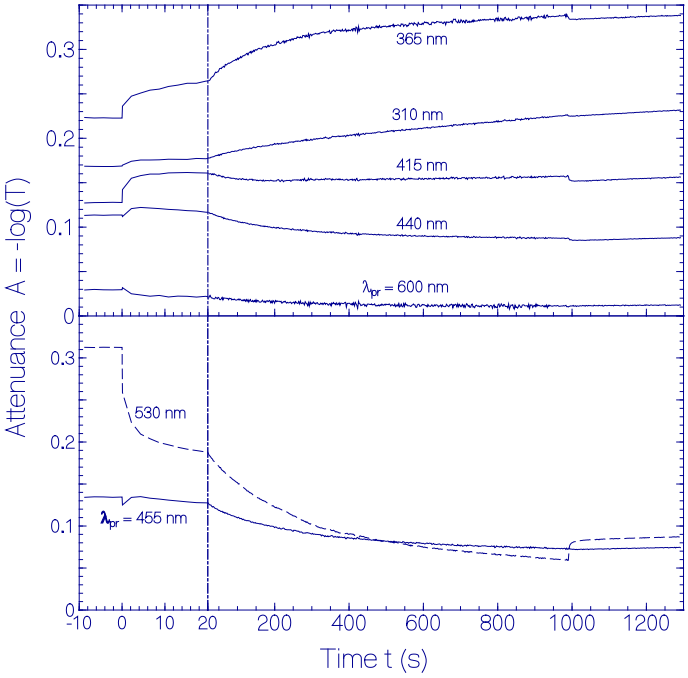


**Fig.6:** Temporal development of the attenuance of Rh (BE) at certain wavelengths (top part: 600 nm, 440 nm, 415 nm, 365 nm, 310 nm; bottom part: 530 nm, 455 nm) before, during, and after light exposure. Excitation wavelength: $\lambda_{exc}$ = 532 nm. Excitation intensity: $I_{exc}$ ≈ 16 mW cm$^{-2}$. Excitation period: $t$ = 0 – 990 s. Data are taken from Fig.5.

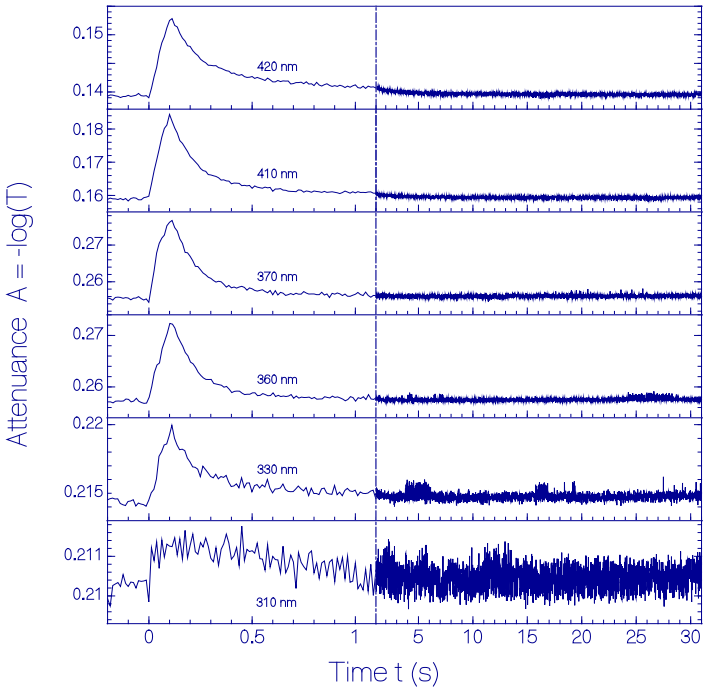


**Fig.7b:** Temporal development of Rh (BE) attenuance at the probe wavelengths 420 nm, 410 nm, 370 nm, 360 nm, 330 nm and 310 nm before, during, and after light exposure. Duration of light exposure is 0.1 s (range from 0 s to 0.1 s). Excitation wavelength $\lambda_{exc}$ = 532 nm. Excitation intensity: $I_{exc}$ ≈ 22 mW cm$^{-2}$. Temperature $\vartheta$ = 21.2±0.2 °C.

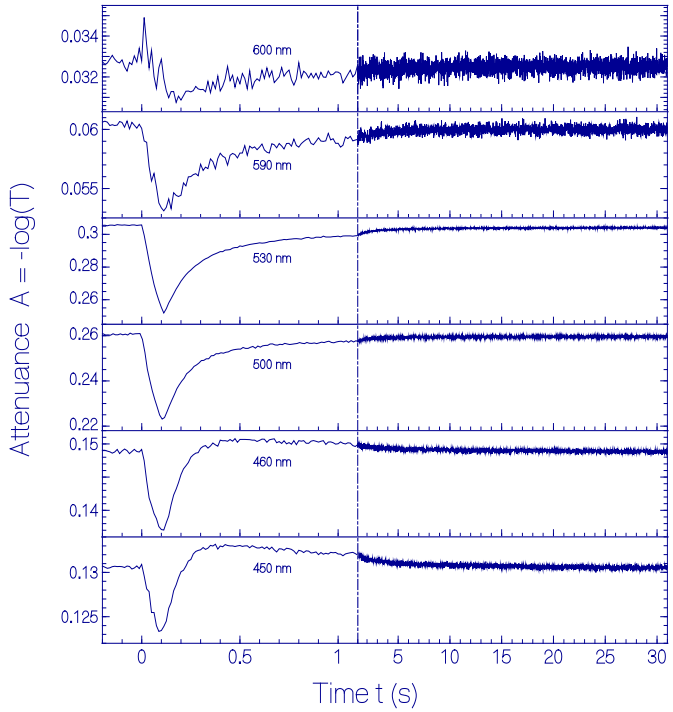


**Fig.7a:** Temporal development of Rh (BE) attenuance at the probe wavelengths 600 nm, 590 nm, 530 nm, 500 nm, 460 nm and 450 nm before, during, and after light exposure. Duration of light exposure is 0.1 s (range from 0 s to 0.1 s). Excitation wavelength $\lambda_{exc}$ = 532 nm. Excitation intensity: $I_{exc}$ ≈ 22 mW cm$^{-2}$. Temperature $\vartheta$ = 21.2±0.2 °C.

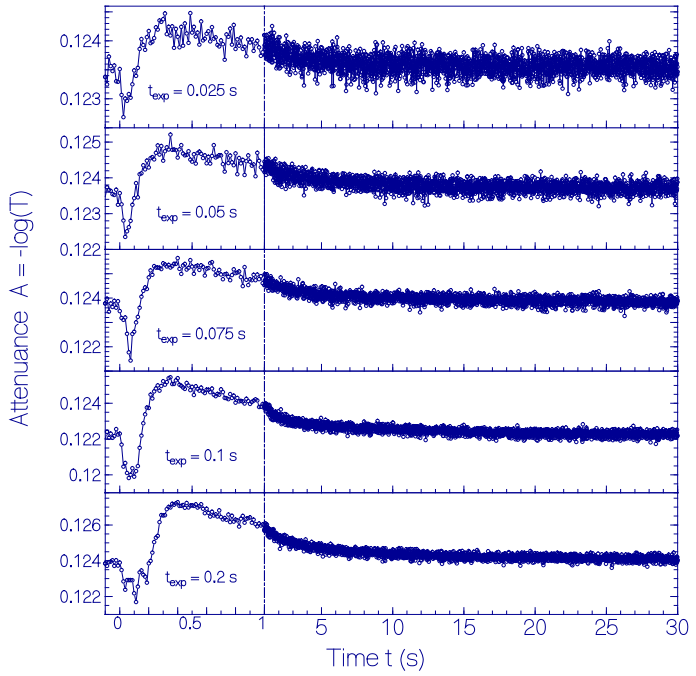


**Fig.8a:** Temporal development of attenuance of Rh (BE) at $\lambda_{pr}$ = 440 nm before, during, and after light exposure at $\lambda_{pr}$ = 532 nm with $I_{exc}$ = 22 mW cm$^{-2}$ for the durations of light exposure of $t_{exp}$ = 0.025 s, 0.05 s, 0.075 s, 0.1 s, and 0.2 s.

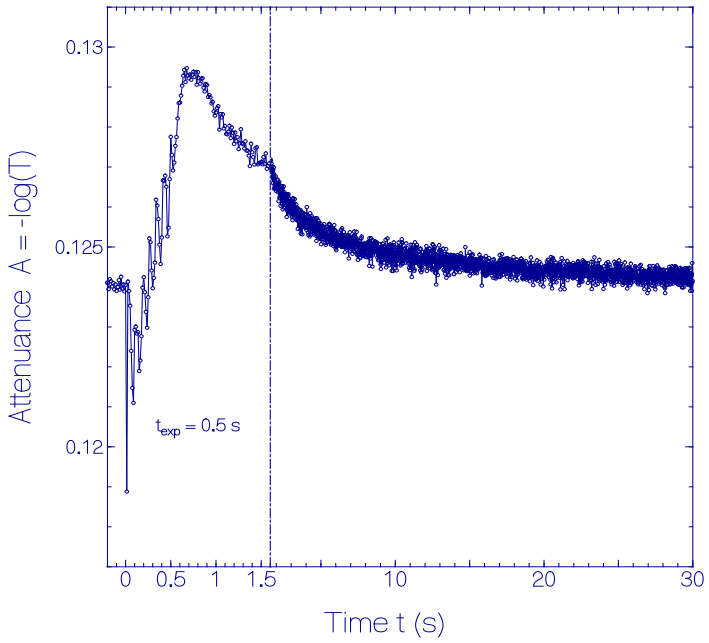


**Fig.8b:** Temporal development of attenuance of Rh (BE) at $\lambda_{pr}$ = 440 nm before, during, and after light exposure at $\lambda_{pr}$= 532 nm with $I_{exc}$ = 22 mW cm$^{-2}$ for the duration of light exposure of $t_{exp}$ = 0.5 s.

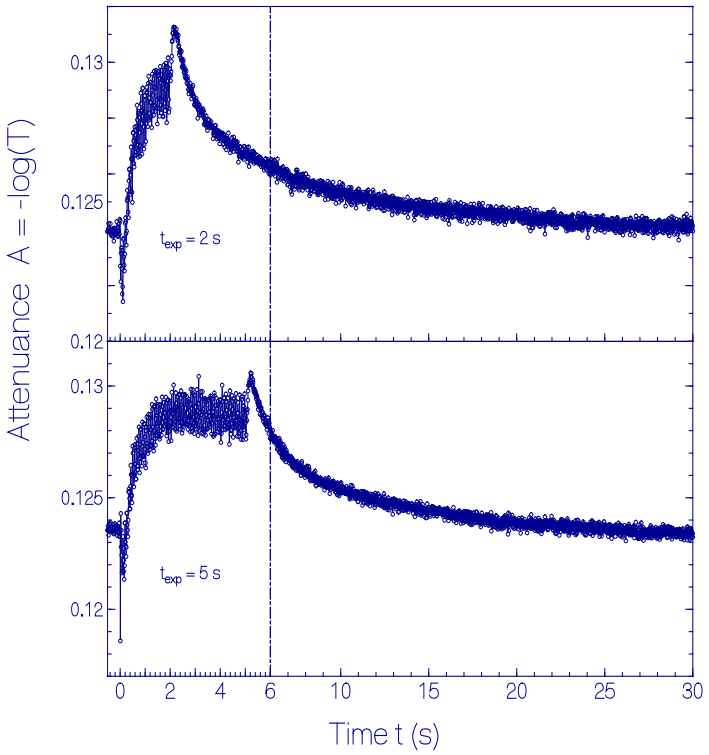


**Fig.8c:** Temporal development of attenuance of Rh (BE) at $\lambda_{pr}$ = 440 nm before, during, and after light exposure at $\lambda_{pr}$= 532 nm with $I_{exc}$ = 22 mW cm$^{-2}$ for the durations of light exposure of $t_{exp}$ = 2 s and 5 s.

temperature. Sample one was exposed for 990 s. During and after light exposure transmission spectra were recorded with a period of 2.171 s in the wavelength range from 600 nm – 310 nm using 5 nm wavelength spacing (see Fig. 5 for some attenuance spectra during exposure (top part) and after exposure (bottom part), and Fig.6 for some temporal attenuance developments at selected probe wavelengths). Sample two was used to study the attenuance kinetics for probe wavelengths in the range from 310 nm to 600 nm in steps of 10 nm in each case over a temporal range of 90 s whereby the light exposure time was set to $t_{exp}$ = 0.1 s (Fig.7a and 7b, exposure from 0 to 0.1 s, presented time range from -0.2 s to 1.1 s and 1.1 s to 31 s). After that the sample two was exposed in a series of time intervals from $t_{exp}$= 0.025 s to 5 s for probing the temporal attenuance development during and after exposure at $\lambda_{pr}$ = 440 nm (Fig.8a-8c).

In Fig.5 attenuance spectra of Rh (BE) before, during (top part) and after (bottom part) light exposure are shown. The thin solid curve in the top part belongs to $t_{exp}$= 0 (measured immediately before light exposure). The sample one was continuously exposed over a period of 990 s. In intervals of 2.171 s attenuance spectra were recorded (curves are shown for the repetition numbers $n$ = 1, 2, 10, 40, 80, 160, 320, 456). The short-dashed spectrum in the top part for $t_{exp}$ = 0.1 s was made up of single-wavelength kinetic measurements of sample two (data adapted from Fig.7).

In the top part of Fig.5 an initially steep and then slowed-down attenuance decrease of the 530 nm absorption band (species Ret_1), a steep rise to a nearly constant absorption around 415 nm (species Ret_3), an initially steep (formation of species Ret_4) and then slowed-down attenuance increase (conversion of species Ret_4 to species Ret_4', see below) of the 365 nm absorption band, and a complex initial absorption decrease followed by an absorption increase and subsequent absorption decrease around 440 nm (species Ret_2) is observed. The bottom part of Fig.5 indicates a small partial – initially fast and then slowed-down – recovery of the 530 nm absorption band (Ret_1) concomitant with a slight absorption decrease of the 365 nm (Ret_4) and 415 nm (Ret_3) absorption bands after light switch-off.

The kinetics of the attenuance development at the onset (time resolution 0.1 s), during (time steps 2.171 s), and after (time steps 2.171 s) light exposure at selected probe wavelengths is depicted in Fig.6 (data are taken from measurements belonging to Fig.5, sample one, and Fig.7, sample two). The dashed curve belonging to $\lambda_{pr}$= 530 nm shows the absorption development of species Ret_1 (likely all-*trans* protonated retinal Schiff base $PRSB^{+}_{trans}$). The attenuation decreased steeply due to photo-isomerization to Ret_5 absorbing around 600 nm (likely all-*trans* protonated retinal Schiff base $PRSB^{+}_{trans}$ isomerization to 13-*cis* protonated retinal Schiff base $PRSB^{+}_{cis}$, see below) which converted to Ret_2 absorbing around 440 nm (likely 3-*cis* protonated retinal Schiff base with repositioned counter ion $PRSB^{+}_{cis,cirp}$, see below), to Ret_3 absorbing around 415 nm (likely all-*trans* protonated retinal Schiff base with re-positioned counter ion $PRSB^{+}_{trans,cirp}$, see below), and to Ret_4 absorbing around 365 nm (likely all-*trans* deprotonated retinal Schiff base $RSB_{trans}$, see below). The decrease of attenuance at 530 nm was leveled off by the fast recovery of the photo-products Ret_2, Ret_3, and Ret_4 to Ret_1 (laser excitation intensity at 532 nm $I_{exc}$ was lower than the saturation intensity $I_{sat}$ necessary for 50 % Ret_1 conversion to photo-products [37-39], see discussion below

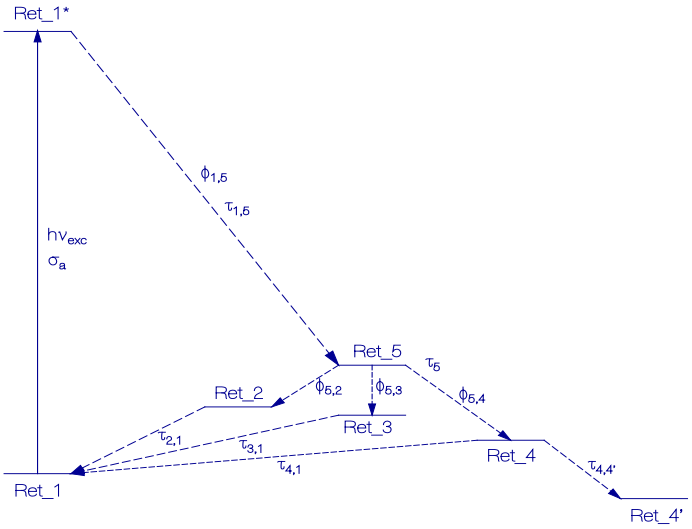


**Fig.9:** Scheme of photo-excitation dynamics of Rh (BE) in the case of excitation of Ret_1. Photo-induced depopulation of Ret_1 by excitation to Ret_1* followed by ultrafast photo-isomerization to Ret_5 ($\tau_{1,5} \approx 1.2$ ps), subsequent population of Ret_2, Ret_3, and Ret_4 from Ret_5 (time constant $\tau_5 \approx 0.1$ s), and ground-state recovery from Ret_2, Ret_3, and Ret_4 to Ret_1 (bi-exponential recovery on sub-second to second timescale). Irreversible formation of Ret_4' from Ret_4 is included (bi-exponential formation with time constants of ≈ 12 s and ≈ 280 s).

with Eq. 14). The attenuance of Ret_1 (530 nm band) continued to decrease with exposure time and the 365 nm absorption band continued to increase because Ret_4 irreversibly converted to Ret_4' (overlapping absorption spectrum around 365 nm, likely change of all-*trans* $RSB_{trans}$ to 13-*cis* $RSB_{cis}$). The whole photo-excitation dynamics of Rh (BE) due to Ret_1 photo-excitation is illustrated in Fig.9.

The temporal attenuance development during light exposure ($\lambda_{exc}$ = 532 nm, $I_{exc} \approx 22$ mW cm$^{-2}$, exposure time $t_{exp} = 0.1$ s) and after light exposure at selected probe wavelengths of $\lambda_{pr}$ = 600 nm, 590 nm, 530 nm, 500 nm, 460 nm, 450 nm, 420 nm, 410 nm, 370 nm, 360 nm, 330 nm, and 310 nm is shown in Fig.7a and Fig.7b. Measurements carried out at $\lambda_{pr}$ = 440 nm for different light exposure times in the range from $t_{exp} = 0.025$ s to $t_{exp} = 5$ s are displayed in Figs.8a-8c. For both Fig.7 and Fig.8 Rh (BE) sample two was used. The time resolution was 0.0125 s. The temperature was $\vartheta = 21.8\pm0.2$ °C.

The initial light-induced attenuance decrease at $\lambda_{pr}$ = 530 nm (Ret_1 species) is analyzed to determine the quantum yield $\phi_{1,5}$ of photo-induced Ret_1 depopulation in the primary photo-cycle of Ret_1 → Ret_5 → Ret_2, Ret_3, Ret_4 → Ret_1. $\phi_{1,5}$ is defined [40] as the ratio of the increment of length-integrated number density $\Delta N_{conv}$ of Ret_1 converted to Ret_5, and subsequently to Ret_2, Ret_3, and Ret_4 to the corresponding increment of absorbed excitation photons $\Delta n_{ph,abs}$, i.e.

$$\phi_{1,5} = \frac{\Delta N_{conv}}{\Delta n_{ph,abs}} \tag{6}$$

The increment of length-integrated number density $\Delta N_{conv}$ is given by

$$\Delta N_{conv} = N_{Ret\_1,0} l_{exc} \frac{\Delta A_{pr}}{A_{pr,0}} \tag{7}$$

where $N_{Ret\_1,0} = \alpha_{Ret\_1,0}(\lambda_{pr})/\sigma_{Ret\_1}(\lambda_{pr})$ is the initial number density of Ret_1, $l_{exc}$ is the sample length in excitation direction, $\Delta A_{pr}$ is the attenuance change at the probe wavelength $\lambda_{pr}$ (here $\lambda_{pr}$ = 530 nm) due to photon absorption $\Delta n_{ph,abs}$, and $A_{pr,0}$ is the initial attenuance at $\lambda_{pr}$. The initial number density of Ret_1 is given by $N_{Ret\_1,0} = \alpha_0(530\text{ nm})/\sigma_{Ret\_1}(530\text{ nm}) \approx A_0(530\text{ nm})\ln(10)/[l_{pr}\sigma_{Ret\_1}(530\text{ nm})] \approx 1.41\times10^{16}$ cm$^{-3}$ ($A_0(530\text{ nm}) = 0.31$, $l_{pr} = 0.3$ cm, $\sigma_{Ret\_1}(530\text{ nm}) = \sigma(530\text{ nm})/\kappa_{Ret\_1} = 1.66\times10^{-16}$ cm$^2$, see Fig.S3). The excitation length is $l_{exc} = 0.15$ cm. For the $\lambda_{Pr}$ = 530 nm curve in Fig. 7a it is $\Delta A_{pr} = 0.01\pm0.001$ for the time increment $\delta t = 0.0125$ s, and the increment of length-integrated number density $\Delta N_{conv}$ becomes $\Delta N_{conv} = (6.9\pm0.7)\times10^{13}$ cm$^{-2}$.

The increment of absorbed excitation photons $\Delta n_{ph,abs}$ in the time increment $\delta t = 0.0125$ s is

$$\Delta n_{ph,abs} = \frac{I_{exc}\delta t}{h\nu_{exc}}\left[1-\exp(-\alpha(\lambda_{exc})l_{exc})\right]. \tag{8}$$

Thereby is $I_{exc} = 0.022\pm0.002$ Wcm$^{-2}$, $\delta t = 0.0125$ s, $h$ is the Planck constant, $\nu_{exc} = c_0/\lambda_{exc} = 5.64\times10^{14}$ Hz ($c_0$ is the speed of light in vacuum), $\alpha(\lambda_{exc}) = \alpha(532\text{ nm}) = A(532\text{ nm})\ln(10)/0.3\text{ cm} = 0.292\times\ln(10)/0.3\text{ cm} = 1.023$ cm$^{-1}$, and $l_{exc} = 0.15$ cm. The resulting increment of absorbed excitation photons is $\Delta n_{ph,abs} = (1.05\pm0.1)\times10^{14}$ cm$^{-2}$.

Insertion of $\Delta N_{conv}$ and $\Delta n_{ph,abs}$ into Eq.6 gives $\phi_{1,5} = 0.66\pm0.15$. This quantum yield indicates that a fraction of 0.66±0.15 of the excited Ret_1 conformation is photo-converted to other rhodopsin conformations (Ret_5, and subsequently to Ret_2, Ret_3, and Ret_4) and a fraction of 0.34±0.15 of the excited Ret_1 rhodopsin recovers in the excited-state isomerization back to its original conformation.

The kinetics of the $\lambda_{pr}$ = 600 nm trace (Ret_5 species) at the top part of Fig.7a indicates a direct photo-isomerization of Ret_1 to Ret_5 (rise of attenuance during the first 0.0125 s of light exposure, the true population time of Ret_5 due to Ret_1 → Ret_5 photo-isomerization is given by the Ret_1 fluorescence lifetime of $\tau_F \approx 1.2$ ps). The Ret_5 population transfers during the light excitation process with a time constant of $\tau_5 \approx 0.1$ s to Ret_2 absorbing around $\lambda_{pr}$ = 440 nm (efficiency $\phi_{5,2}$), to Ret_3 absorbing around 415 nm (efficiency $\phi_{5,3}$), and to Ret_4 absorbing around 365 nm (efficiency $\phi_{5,4}$). The long-time increase of attenuance at $\lambda_{pr}$ = 600 nm is determined by the absorption recovery of Ret_1 (the absorption band of Ret_1 extends out to $\lambda > 600$ nm).

The initial attenuance decrease at 440 nm belongs to the attenuance decrease of the broad 530 nm Ret_1 absorption band. The following rise of attenuance is due to Ret_5 conversion to Ret_2. An attenuance plateau built up due to the continued filling of Ret_2 from Ret_5 and the depopulation of Ret_2 to Ret_1. The steep rise of attenuance at $\lambda_{pr}$ = 440 nm at the moment of light switch-off followed the attenuance rise at $\lambda_{pr}$ = 530 nm and belongs to the

broad Ret_1 absorption band dynamics (Ret_1 recovery from Ret_3 and Ret_4, see Fig.9). Finally the $\lambda_{pr}$ = 440 nm attenuance (Ret_2) recovered after excitation switch-off bi-exponentially with the time constants $\tau_{2,1,f} \approx 0.75$ s (fraction $\chi_{2,1,f} \approx 0.8$) and $\tau_{2,1,sl} \approx 11$ s (fraction $\chi_{2,1,sl} \approx 0.2$) due to Ret_2 to Ret_1 conversion (relaxation from Ret_2 to Ret_1 via Ret_3 cannot be excluded).

After excitation light switch-off also Ret_3 and Ret_4 converted approximately bi-exponential to Ret_1 according to

$$N_{Ret\_i} \approx N_{Ret\_i,0}\left[\chi_{i,1,f}\exp\left(-\frac{t}{\tau_{i,1,f}}\right)+\chi_{i,1,sl}\exp\left(-\frac{t}{\tau_{i,1,sl}}\right)\right]. \quad (9)$$

Likely two different Rh (BE) protein conformations are present with fast and slow retinal relaxation dynamics. The determined relaxation parameters for Ret_3 are $\tau_{3,1,f} \approx 0.15$ s ($\chi_{3,1,f} \approx 0.86$) and $\tau_{3,1,sl} \approx 1.3$ s ($\chi_{3,1,sl} \approx 0.14$) (see the kinetic attenuance traces at $\lambda_{pr}$ = 420 nm and $\lambda_{pr}$ = 410 nm in Fig.7b). The determined relaxation parameters for Ret_4 are $\tau_{4,1,f} \approx 0.15$ s ($\chi_{4,1,f} \approx 0.89$) and $\tau_{4,1,sl} \approx 1.35$ s ($\chi_{4,1,sl} \approx 0.11$) (see the kinetic attenuance traces at $\lambda_{pr}$ = 370 nm and $\lambda_{pr}$ = 360 nm in Fig.7b). The parameters are collected in Table 2. The population of Ret_4 leaked out to irreversible Ret_4' formation.

The long-time secondary photo-excitation dynamics of Ret_1 (Fig.6) fits to a continuously slowed down attenuance decrease at $\lambda_{pr}$ = 530 nm (Ret_1 photo-conversion) and a continuously slowed down attenuance increase at $\lambda_{pr}$ = 365 nm (formation of irreversible Ret_4' from Ret_4). The attenuance development during exposure at $\lambda_{pr}$ = 530 nm and $\lambda_{pr}$ = 365 nm fits well to a three-term exponential dependence according to

$$A_i(t_{exp}) = A_{i,0} + \delta A_i \sum_{j=1}^{3} \kappa_{i,j}\left[1-\exp\left(-\frac{t_{exp}}{\tau_j}\right)\right] \quad (10)$$

with the parameters for $i$ = 530 nm: $A_{530nm,0}$ = 0.313, $\delta A_{530nm}$ = -0.254, $\kappa_{530nm,1}$ = 0.34, $\kappa_{530nm,2}$ = 0.14, $\kappa_{530nm,3}$ = 0.52, the parameters for $i$ = 365 nm: $A_{365nm,0}$ = 0.223, $\delta A_{365nm}$ = 0.12, $\kappa_{365nm,1}$ = 0.17, $\kappa_{365nm,2}$ = 0.21, $\kappa_{365nm,3}$ = 0.62, and the common time constants $\tau_1$ = 0.15 s, $\tau_2$ = 12 s, and $\tau_3$ = 280 s.

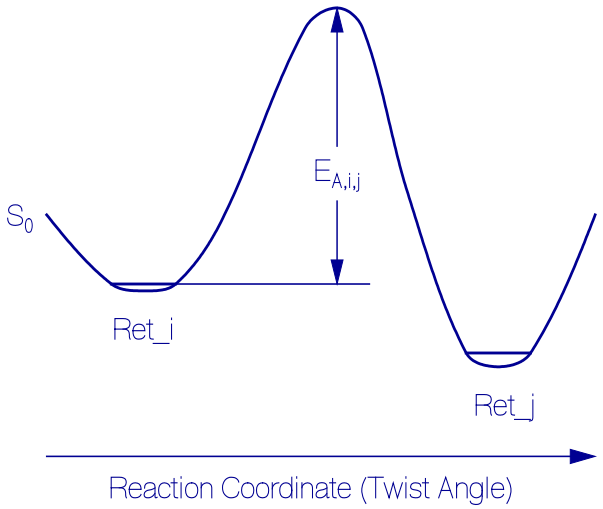


**Fig.10a:** Schematic apparent ground-state potential energy surface between Ret_i and Ret_j. $E_{A,i,j}$: energy barrier between Ret_i and Ret_j.

In the primary photo-cycle of Ret_1→Ret_5→Ret_2, Ret_3, Ret_4→Ret_1 a steady-state level population density (attenuance) of Ret_1, Ret_5, Ret_2, Ret_3, Ret_4 is built up. The steady-state equilibrium is disturbed by the leaking out of the Ret_4 population to Ret_4' which causes a secondary photo-dynamics with depopulation of Ret_1 and committing depopulation of Ret_5, Ret_2, Ret_3, Ret_4 (steady-state level population re-adjustment) and continued irreversible Ret_4' population density build-up.

The final attenuance situation of Ret_1 and Ret_4' is thought to be determined by thermal equilibrium population of the ground-state energy levels of Ret_4' and Ret_1. An approximate value of the photo-degraded energy level position of Ret_4' may be obtained from the attenuation ratio $A$(370 nm)/$A$(530 nm) after long-time sample exposure of Fig.5. There it is $\kappa_{Ret\_4'}/\kappa_{Ret\_1} \approx A$(370 nm, $t_{exp}$ = 990 s)/$A$(530 nm, $t_{exp}$ = 990 s) ≈ 5.7 giving (Eq.5 with $\vartheta$ = 21.2 °C) $E_{4',1} \approx -7.1\times10^{-21}$ J ($\tilde{\nu}_{4',1} \approx -355$ cm$^{-1}$), i.e. Ret_4' is energetically located ≈ 355 cm$^{-1}$ below the energetic level of Ret_1.

The relaxation times $\tau_{2,1,f}$, $\tau_{2,1,sl}$, $\tau_{3,1,f}$, $\tau_{3,1,sl}$, $\tau_{4,1,f}$, $\tau_{4,1,sl}$, and $\tau_{4,4',f}$, $\tau_{4,4',sl}$ indicate ground-state potential barriers between the species Ret_2, Ret_3, Ret_4, Ret_1 and Ret_4' as schematically illustrated in Fig.10a between states $i$ and $j$ ($i$ = 2, 3, 4, $j$ = 1, 4'). The relation between the relaxation times $\tau_{i,j}$ (relaxation rates $k_{i,j} = \tau_{i,j}^{-1}$) and the potential energy activation barrier $E_{A,i,j} = hc_0\tilde{\nu}_{A,i,j}$ is given by the Arrhenius relation [41]

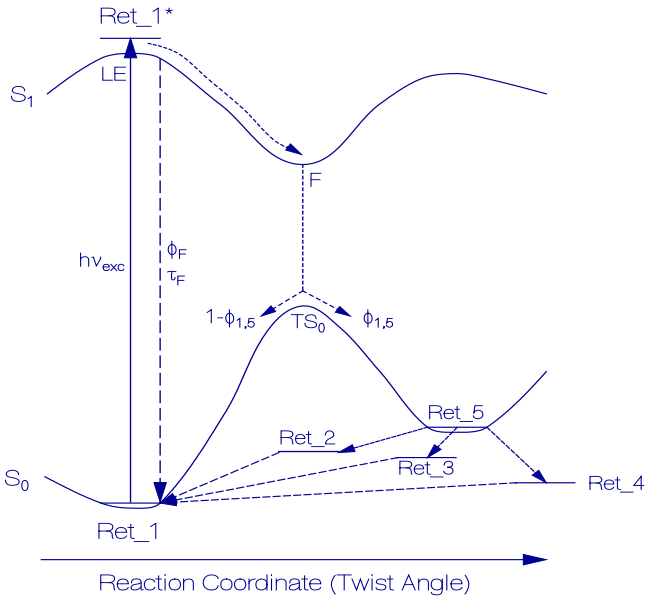


**Fig.10b:** Schematic reaction coordinate diagram for photo-isomerization of Ret_1 to Ret_5 on a picosecond timescale, and sub-second conversion of Ret_5 to Ret_2, Ret_3, and Ret_4 followed by sub-second to second recovery of Ret_2, Ret_3, Ret_4 to Ret_1 (primary photo-cycle). LE: locally excited state on $S_1$ potential energy surface. F: funnel (conical intersection position). $TS_0$: transition state of $S_0$ potential energy surface.

**Table 2:** Photo-dynamics parameters of Rh (BE) in the case of Ret_1 photo-excitation.

| Parameter | Value | Comments |
|---|---|---|
| *Quantum yields* | | |
| $\phi_{1,5}$ | 0.66±0.15 | Eqs.6-8 |
| $\phi_{5,2}$ | ≈ 0.14 | $\phi_{5,2} \approx \frac{\delta A_{440nm,ini}}{\delta A_{440nm,ini} + \delta A_{415nm,ini} + \delta A_{365nm,}}$ |
| $\phi_{5,3}$ | ≈ 0.43 | $\phi_{5,3} \approx \frac{\delta A_{415nm,ini}}{\delta A_{440nm,ini} + \delta A_{415nm,ini} + \delta A_{365nm,}}$ |
| $\phi_{5,4}$ | ≈ 0.43 | $\phi_{5,4} \approx \frac{\delta A_{365nm,ini}}{\delta A_{440nm,ini} + \delta A_{415nm,ini} + \delta A_{365nm,}}$ |
| *Relaxation times* $\tau_{i,j}$ *[and activation barriers* $\tilde{\nu}_{A,i,j}$ *]* | | |
| $\tau_{1,5}$ (ps) | ≈ 1.2 | $\tau_{1,5} = \tau_{F,Ret\_1}$ |
| $\tau_5$ (s) | ≈ 0.1 | Fit to Fig.7 curves |
| $\chi_{2,1,f}$ | ≈ 0.8 | Fit to Fig.8a, 0.1 s curve |
| $\tau_{2,1,f}$ (s), [$\tilde{\nu}_{A,2,1,f}$ (cm$^{-1}$)] | ≈ 0.74, [5958] | Fit to Fig.8a, 0.1 s curve |
| $\chi_{2,1,sl}$ | ≈ 0.2 | Fit to Fig.8a, 0.1 s curve |
| $\tau_{2,1,sl}$ (s), [$\tilde{\nu}_{A,2,1,sl}$ (cm$^{-1}$)] | ≈ 11, [≈ 6510] | Fit to Fig.8a, 0.1 s curve |
| $\overline{\tau}_{2,1}$ (s) | ≈ 0.91 | $\overline{\tau}_{2,1}^{-1} = \chi_{2,1,f}\tau_{2,1,f}^{-1} + \chi_{2,1,sl}\tau_{2,1,sl}^{-1}$ |
| $\chi_{3,1,f}$ | ≈ 0.86 | Fit to Fig.7b, 420 nm and 410 nm curves |
| $\tau_{3,1,f}$ (s), [$\tilde{\nu}_{A,3,1,f}$ (cm$^{-1}$)] | ≈ 0.15, [5632] | Fit to Fig.7b, 420 nm and 410 nm curves |
| $\chi_{3,1,sl}$ | ≈ 0.14 | Fit to Fig.7b, 420 nm and 410 nm curves |
| $\tau_{3,1,sl}$ (s), [$\tilde{\nu}_{A,3,1,sl}$ (cm$^{-1}$)] | ≈ 1.3, [6073] | Fit to Fig.7b, 420 nm and 410 nm curves |
| $\overline{\tau}_{3,1}$ (s) | ≈ 0.171 | $\overline{\tau}_{3,1}^{-1} = \chi_{3,1,f}\tau_{3,1,f}^{-1} + \chi_{3,1,sl}\tau_{3,1,sl}^{-1}$ |
| $\chi_{4,1,f}$ | ≈ 0.89 | Fit to Fig.7b, 370 nm and 360 nm curves |
| $\tau_{4,1,f}$ (s), [$\tilde{\nu}_{A,4,1,f}$ (cm$^{-1}$)] | ≈ 0.15, [≈ 5632] | Fit to Fig.7b, 370 nm and 360 nm curves |
| $\chi_{4,1,sl}$ | ≈ 0.11 | Fit to Fig.7b, 370 nm and 360 nm curves |
| $\tau_{4,1,sl}$ (s), ), [$\tilde{\nu}_{A,4,1,sl}$ (cm$^{-1}$)] | ≈ 1.35, [≈ 6081] | Fit to Fig.7b, 370 nm and 360 nm curves |
| $\overline{\tau}_{4,1}$ (s) | ≈ 0.166 | $\overline{\tau}_{4,1}^{-1} = \chi_{4,1,f}\tau_{4,1,f}^{-1} + \chi_{4,1,sl}\tau_{4,1,sl}^{-1}$ |
| $\chi_{4,4',f}$ | ≈ 0.21 | Fit to Fig.6, 365 nm curve |
| $\tau_{4,4',f}$ (s), [$\tilde{\nu}_{A,4,4',f}$ (cm$^{-1}$)] | ≈ 12, [6528] | Fit to Fig.6, 365 nm curve |
| $\chi_{4,4',sl}$ | ≈ 0.79 | Fit to Fig.6, 365 nm curve |
| $\tau_{4,4',sl}$ (s), [$\tilde{\nu}_{A,4,1,sl}$ (cm$^{-1}$)] | ≈ 280, [7172] | Fit to Fig.6, 365 nm curve |
| $\chi_{rec,1,f}$ | ≈ 0.82 | Fit to Fig.7a, 530 nm curve |
| $\tau_{rec,1,f}$ (s) | ≈ 0.16 | Fit to Fig.7a, 530 nm curve |

| | | |
|---|---|---|
| $\chi_{rec,1,sl}$ | ≈ 0.18 | Fit to Fig.7a, 530 nm curve |
| $\tau_{rec,1,sl}$ (s) | ≈ 1.3 | Fit to Fig.7a, 530 nm curve |
| *Saturation intensity* | | |
| $I_{sat}$ (W cm$^{-2}$) | ≈ 0.018 | $I_{sat} = \frac{h\nu_{exc}}{\sigma_{a,exc}\tau_{rec,1}\phi_{conv}}$ |
| *Ret_1 absorption recovery time* | | |
| $\tau_{rec,1}$ (s) | ≈ 0.19 | $\tau_{rec,1}^{-1} \approx \chi_{rec,1,f}\tau_{rec,1,f}^{-1} + \chi_{rec,1,sl}\tau_{rec,1,sl}^{-1}$ |
| *Excitation absorption cross-section* | | |
| $\sigma_{a,exc}$ (cm$^2$) | $1.66\times10^{-16}$ | Fig.S3, $\sigma_{a,exc} = \sigma_a(532\text{ nm})/\kappa_{Ret\_1}$ |

$$k_{i,j} = \tau_{i,j}^{-1} = \nu_0 \exp\left(-\frac{E_{A,i,j}}{k_B\vartheta}\right) = \nu_0 \exp\left(-\frac{hc_0\tilde{\nu}_{A,i,j}}{k_B\vartheta}\right) \quad (11a)$$

where $\nu_0 \approx k_B\vartheta/h$ is the attempt frequency of barrier crossing [22,36], $h$ is the Planck constant, $k_B$ is the Boltzmann constant, and $\vartheta$ is the temperature in Kelvin (here $\vartheta$ = 294.35 K = 21.2 °C for Figs.5-8 giving $\nu_0 = 6.13\times10^{12}$ s$^{-1}$). Solving Eq.11a for activation barrier wavenumber $\tilde{\nu}_{A,i,j}$ gives

$$\tilde{\nu}_{A,i,j} = -\frac{k_B\vartheta}{hc_0}\ln(\tau_{i,j}\nu_0) = \frac{\nu_0}{c_0}\ln(\tau_{i,j}\nu_0) \quad (11b)$$

For the determined $\tau_{i,j}$ values listed in Table 2 the corresponding activation barrier wavenumbers $\tilde{\nu}_{A,i,j}$ are calculated by use of Eq.11b. The obtained values are included in Table 2.

## 4. Discussion

Absorption and fluorescence studies of fresh thawed samples, thermal degradation studies, absorption spectroscopic primary photo-cycle dynamics and long-time light exposure secondary photo-conversion dynamics investigations have been carried out. They revealed i) a composition of several retinal species, ii) a thermal species re-composition, iii) a photo-induced cyclic rhodopsin re-structuring, and iv) a long-time photo-induced irreversible deprotonation of initially protonated retinal Schiff base of Rh (BE).

Rhodopsin species (retinal species in opsin protein environment) resolved in the absorption, fluorescence and photo-dynamics studies with proposed retinal structures are listed in Table 3. The photo-cycle dynamics of Rh (BE) was only studied for the retinal species Ret_1 (likely all-*trans* protonated retinal Schiff base). The time resolution of this photo-cycle dynamics study was 0.0125 s. The absorption and fluorescence spectral shapes of retinals in rhodopsins depend on the retinal protonation stage and the charge distribution in the amino acid environment around the retinal in the rhodopsin protein [10,11,42-47].

**Table 3:** Resolved retinal species in Rh (BE)

| Species name | Proposed structure | Peak absorption wavelength $\lambda_A$ (nm) | |
|---|---|---|---|
| | | Fresh | Denatured |
| Ret_1 | All-*trans* protonated retinal Schiff base $PRSB^+_{trans}$ | 530 | 530 |
| Ret_2 | 13-*cis* protonated retinal Schiff base with counter ion repositioned $PRSB^+_{cis,cirp}$ | 440 | 480 |
| Ret_3 | All-*trans* protonated retinal Schiff base with counter ion repositioned $PRSB^+_{trans,cirp}$ | 415 | 450 |
| Ret_4 | Retinal Schiff base RSB (unexposed, and primary photopoduct) | 360 (likely all-*trans*) | |
| Ret_4' | Retinal Schiff base RSB (denatured, and secondary photoproduct) | 368 (likely 13-*cis*) | 380 (likely 13-*cis*) |
| Ret_5 | 13-*cis* protonated retinal Schiff base $PRSB^+_{cis}$ | ≈ 600 | ≈ 670 |

The presence of dark-adapted ground-state rhodopsin isoforms with thermal equilibration between all-*trans* retinal and 13-*cis* retinal is a common feature of microbial rhodopsins (see [48-50] for bacteriorhodopin, [51] for proteorhodopsin, [52] for halorhodopsin, [53] for *Anabaena* sensory rhodopsin, [13] for histidine kinase rhodopsin HKR1 from *Chlamydomonas reinhardtii*). Here for Rh (BE) four retinal species were resolved in freshly thawed samples (Ret_1, Ret_2, Ret_3, Ret_4) and a temperature dependent gradual partial conversion of protonated retinal Schiff bases Ret_1, Ret_2, Ret_3 and deprotonated retinal Schiff base Ret_4 to deprotonated retinal Schiff base Ret_4' was observed.

### 4.1. Ultrafast Photo-Dynamics of Rh (BE)

Fluorescence excitation wavelength dependent recording of fluorescence quantum distributions of Rh (BE) revealed the presence of at least four retinal species (Ret_1, Ret_2, Ret_3, Ret_4) in fresh thawed Rh (BE) samples.

For Ret_1 (likely all-*trans* protonated retinal Schiff base) the determined Strickler-Berg based fluorescence lifetime of $\tau_F \approx 1.2$ ps indicates barrier-less relaxation of the excited retinal species in the surrounding protein conformation from the locally excited state (LE) along the excited-state reaction coordinate (twist angle) leading to a funnel (F, conical intersection [30], seam of intersection [54]). There efficient internal conversion from the excited state of the species (F) to the ground state potential energy surface of the species (transition state $TS_0$) takes place with partial recovery of the initial configuration (educt state) and partial relaxation to an isomer configuration (intermediate product state, see illustrations of Fig.9 and Fig.10b) [11]. Here the photo-isomerization is thought to be all-*trans* protonated retinal Schiff base $PRSB^+_{trans}$(Ret_1) to 13-*cis* protonated retinal Schiff base $PRSB^+_{cis}$ (Ret_5) isomerization. Such barrier-less relaxation of excited retinal in rhodopsin was observed in most animal (type-II) rhodopsins [55] and microbial (type-I) rhodopsins (proteorhodopsin [56], bacteriorhodopsin [57], halorhodopsin [58], sensory rhodopsin SR II [59], channelrhodopsin-2 [60], *Anabaena* sensory rhodopsin [61]).

For Ret_2 (likely 13-*cis* protonated retinal Schiff base with re-positioned counter ion), Ret_3 (likely all-*trans* protonated retinal Schiff base with re-positioned counter ion) and Ret_4 (likely deprotonated all-*trans* retinal Schiff base) Strickler-Berg based fluorescence lifetimes of $\tau_{F,Ret\_2} \approx 8.9$ ps, $\tau_{F,Ret\_3} \approx 20$ ps, and $\tau_{Ret\_4} \approx 1.4$ ps were determined. These fluorescence lifetimes were shortened by Förster-type energy transfer (see above, intrinsic fluorescence lifetimes without Förster-type energy transfer, $\tau_{F,0,Ret\_2}$, $\tau_{F,0,Ret\_3}$ and $\tau_{F,0,Ret\_4}$, are expected to be in the hundred picosecond range). The long excited-state lifetimes indicate excited state relaxation to funnels for $S_1$-$S_0$ internal conversion via potential barriers [13,31]. Such excited-state potential barrier slowed-down relaxation of excited retinals in rhodopsins was previously observed for sensory rhodopsin SR I from *Halobacter salarium* [59] and histidine kinase rhodopsin HKR1 from *Chlamydomonas reinhardtii* [12,13].

The excitation wavelength dependent fluorescence emission studies in the short-wavelength region ($\lambda_{F,exc} < 330$ nm) indicated dominant Trp fluorescence emission of the apoprotein (Apo, fluorescence peak around $\lambda_F \approx 330$ nm). The observed Strickler-Berg based fluorescence lifetime of $\tau_{F,Apo} \approx 410$ ps indicates a Förster-type fluorescence quenching [18] (resonance energy transfer by long-range dipole-dipole Coulomb interaction [25]). The Trp fluorescence quantum yield in neutral aqueous solution is $\phi_F = 0.13$ [32-34] and the fluorescence decay in neutral aqueous solution is bi-exponential with a small component of lifetime of 0.5 ns and dominant component of lifetime of 2.78 ns [62].

### 4.2. Photo-Cycling and Photo-Conversion Dynamics of Rh (BE) in the Case of Ret_1 Excitation

The photo-dynamics of Rh (BE) in the case of excitation at $\lambda_{exc} = 532$ nm, where Ret_1 is absorbing, was presented above (Figs.5-8) with time resolution of 0.0125 s. The relaxation dynamics after photo-excitation is illustrated in Fig.9 and Fig.10b. From the local excited state LE of Ret_1 it occurs fast barrier-less relaxation to the $S_1$-state funnel position F with internal conversion to the $S_0$ transition-state position $TS_0$ (relaxation time $\tau_{1,5} = \tau_{F,Ret\_1} \approx 1.2$ ps). From there occurs back-transfer to the original educt state Ret_1 (quantum efficiency $1 - \phi_{1,5} \approx 0.34$) and transfer to the isomer Ret_5 (quantum efficiency $\phi_{1,5} \approx 0.66$). The species Ret_5 has a lifetime of $\tau_5 \approx 0.1$ s. It converts to Ret_2 (conversion efficiency $\phi_{5,2} \approx 0.14$), Ret_3 ($\phi_{5,3} \approx 0.43$), and Ret_4 ($\phi_{5,4} \approx 0.43$). Ret_2, Ret_3, and Ret_4 recovered bi-exponentially back to Ret_1 with the time constants (and fractions) $\tau_{2,1,f} \approx 0.74$ s ($\chi_{2,1,f} \approx 0.8$), $\tau_{2,1,sl} \approx 11$ s ($\chi_{2,1,sl} \approx 0.2$), $\tau_{3,1,f} \approx 0.15$ s ($\chi_{3,1,f} \approx 0.86$), $\tau_{3,1,sl} \approx 1.3$ s ($\chi_{3,1,sl} \approx 0.14$), $\tau_{4,1,f} \approx 0.15$ s ($\chi_{2,1,f} \approx 0.89$), and $\tau_{4,1,sl} \approx 1.35$ s ($\chi_{4,1,sl} \approx 0.11$). This described dynamics is the primary photo-cycling of Rh (BE) in the case of Ret_1 excitation.

This primary photo-cycling does not occur in a fully closed cycle since Ret_4 leaks out to the formation of irreversible Ret_4'. This leaking out of Ret_4 to Ret_4' during long-time sample exposure with the time constants of $\tau_{4,4',f} \approx 12$ s ($\chi_{4,4',f} \approx 0.21$) and $\tau_{4,4,sl} \approx 280$ s ($\chi_{4,4',sl} \approx 0.79$) destroys the excitation intensity dependent steady-state Ret_1, Ret_2, Ret_3, Ret_4 species mole-fraction distribution of the primary photo-cycle towards continuous Ret_1, Ret_2, Ret_3, Ret_4 species mole-fraction reduction and continued Ret_4' mole-fraction increase in a secondary photo-excitation dynamics. An energy level scheme of the primary photo-cycle dynamics is shown in Fig.9 and Fig.10b, and the secondary photo-excitation dynamics due to Ret_4 → Ret_4' conversion is included in Fig.9.

The branching quantum efficiencies of conversion of Ret_5 to Ret_2 ($\phi_{5,2}$), Ret_3 ($\phi_{5,3}$), and Ret_4 ($\phi_{5,4}$) may be approximately determined from the initial attenuation changes $\delta A$ at the probe wavelengths $\lambda_{pr}$ = 440 nm (Ret_2), 415 nm (Ret_3), and 365 nm (Ret_4) according to

$$\phi_{5,2} \approx \frac{\delta A_{440nm,ini}}{\delta A_{440nm,ini} + \delta A_{415nm,ini} + \delta A_{365nm,ini}} \qquad (12a)$$

$$\phi_{5,3} \approx \frac{\delta A_{415nm,ini}}{\delta A_{440nm,ini} + \delta A_{415nm,ini} + \delta A_{365nm,ini}} \quad (12b)$$

$$\phi_{5,4} \approx \frac{\delta A_{365nm,ini}}{\delta A_{440nm,ini} + \delta A_{415nm,ini} + \delta A_{365nm,ini}} \quad (12c)$$

The obtained conversion efficiencies are $\phi_{5,2} \approx 0.14$, $\phi_{5,3} \approx 0.43$, and $\phi_{5,4} \approx 0.43$. These parameters are collected in Table 2.

The primary photo-cycling turnover $\kappa_{pc}$ (ratio of attenuance decrease at 530 nm within $t_{exp} \approx 3\times\tau_{rec,1,sl}$, $\delta A_{530\,nm,ini}$, to attenuance at 530 nm before light exposure, $A_{530\,nm,ini}$) is limited by the applied excitation light intensity $I_{exc}$ compared to the saturation intensity $I_{sat}$ according to (see appendix of [39])

$$\kappa_{pc} = \frac{\delta A_{530\,nm,ini}}{A_{530\,nm,ini}} \approx \frac{I_{exc}/I_{sat}}{1 + I_{exc}/I_{sat}} \quad (13)$$

where the saturation intensity is given by

$$I_{sat} = \frac{h\nu_{exc}}{\sigma_{a,exc}\tau_{rec,1}\phi_{conv}} \quad (14)$$

with

$\tau_{rec,1}^{-1} \approx \chi_{rec,1,f}\tau_{rec,1,f}^{-1} + \chi_{rec,1,sl}\tau_{rec,1,sl}^{-1}$. A value of $I_{sat} \approx 18$ mW cm$^{-2}$ is determined using $\sigma_{a,exc} = 1.66\times10^{-16}$ cm$^2$, $\tau_{rec,1} = 0.19$ s. and $\phi_{conv} \approx 0.66$.

The photo-cycling dynamics of Ret_1 of Rh (BE) (Fig.9, Fig.10b) is similar complex as observed in other microbial rhodopsins where the photo-excitation results in photo-cycles involving intermediate states and performing biochemical actions like ion pumping [63-67], channel opening [10,68-70], sensing [53,71], and photo-switching [12,13,53,61,72,73].

## 5. Conclusions

The rhodopsin part Rh (BE) of the rhodopsin-guanylyl cyclase RhGC of the aquatic fungus *Blastocladiella emersonii* was studied by absorption and emission spectroscopic methods. It was found that fresh thawed Rh (BE) was composed of a mixture of retinal – protein conformations. The resolved retinal conformations are likely all-*trans* protonated retinal Schiff base PRSB$^+_{trans}$(Ret_1, peak wavelength position $\lambda_{Ret\_1} \approx 529$ nm), 13-*cis* protonated retinal Schiff base with repositioned counter ion PRSB$^+_{cis,cirp}$ (Ret_2, $\lambda_{Ret\_2} \approx$ 440 nm), all-*trans* protonated retinal Schiff base with repositioned counter ion PRSB$^+_{trans,cirp}$ (Ret_3, $\lambda_{Ret\_3} \approx 415$ nm), and all-*trans* deprotonated retinal Schiff base RSB$_{trans}$ (Ret_4, $\lambda_{Ret\_4} \approx 360$ nm).

The Rh (BE) thermal stability was found to be rather low. An apparent protein melting temperature of $\vartheta_m \approx 49$ °C was determined. The apparent protein melting time at room temperature (≈ 21.9 °C) was $t \approx 1.45$ h. The enthalpy and entropy of the irreversible protein unfolding of Rh (BE) were determined (section S6.3 of Supporting material).

The $S_0 \rightarrow S_1$ photo-excitation of Ret_1 (PRSB$^+_{trans}$) caused Ret_1* conversion to Ret_5 (likely 13-*cis* protonated retinal Schiff base PRSB$^+_{cis}$ ($\lambda_{Ret\_5} \approx 600$ nm, process: excited-state all-*trans* – 13-*cis* isomerization) within the excited-state lifetime of $\tau_F \approx 1.2$ ps with a quantum efficiency of $\phi_{1,5} = 0.66\pm0.15$. Ret_5 converted on a time scale of $\tau_5 \approx 0.1$ s to Ret_2 (likely 13-*cis* protonated retinal Schiff base with counter ion repositioned PRSB$^+_{cis,cirp}$, process: charge redistribution), Ret_3 (likely all-*trans* protonated retinal Schiff base with repositioned counter ion PRSB$^+_{trans,cirp}$, process: *cis-trans* isomerization with charge redistribution), and to Ret_4 (likely deprotonated all-*trans* retinal Schiff base RSB$_{trans}$, process: *cis-trans* isomerization and de-protonation). The generated photo-excitation products, Ret_5, Ret_2, Ret_3, and Ret_4, recovered back to Ret_1 establishing the primary Ret_1 → Ret_5 → Ret_2, Ret_3, Ret_4 → Ret_1 photo-cycle dynamics. Two protein conformations were resolved: one with fast photo-cycling period of $\tau_{rec,1,f} \approx 0.16$ s (fraction ≈ 0.82) and one with slow photo-cycling period of $\tau_{rec,1,sl} \approx 1.3$ s (fraction ≈ 0.18).

In long-time Ret_1 photo-excitation the photo-generated Ret_4 (likely all-*trans* retinal Schiff base RSB$_{trans}$) converted irreversibly to Ret_4' (likely 13-*cis* retinal Schiff base RSB$_{cis}$) in a ground-state *trans* – *cis* isomerization process causing the above described secondary Ret_1 photo-excitation dynamics.

In the photo-activated guanylyl cyclase activity studies using the rhodopsin-guanylyl cyclase RhGC of *Blastocladiella emersonii* [7] the photo-generated deprotonated chromophore P380 (here named Ret_4) was thought to be the rhodopsin signaling state of RhGC driving the guanylyl cyclase activity of converting guanosine triphosphate (GTP) to 3' ,5'-cyclic guanosine monophosphate (cGMP). Considering the complex primary photo-cycle (Fig.9 and Fig.10b) and secondary photo-conversion dynamics (included in Fig.9) of Rh (BE) no predestinated role of Ret_4 is seen. It seems likely that the non-radiative local excitation energy release in Rh (BE) (mainly in the photo-isomerization of Ret_1 to Ret_5) drives the guanylyl cyclase activity in RhGC. A likely mechanism of regulation of the guanylyl cyclase activity involves a light-induced reorientation of Rh (BE) that abolishes steric cyclase blockage in the homodimer [74-76]. Such domain realignment would not require the presence of a signaling state *per se*. A further indication for the concept of regulation by reorientation is that isolated cyclase domains are constitutively active (Katja Stehfest, personal communication).

## Acknowledgements

We thank Christina Schnick, Humboldt Universität zu Berlin, for excellent technical assistance. A. P. thanks Prof. F. J. Gießibl, University of Regensburg, for his kind hospitality. The work was supported by the ERC (project MERA to P.H.).

## Supplementary Material to Absorption and Emission Spectroscopic Investigation of Thermal Dynamics and Photo-Dynamics of the Rhodopsin Domain of the Rhodopsin-Guanylyl Cyclase from the Aquatic Fungus *Blastocladiella emersonii*

### S1. Amino acid sequence of the rhodopsion part Rh (BE) of the rhodopsin-guanylyl cyclase of *Blastocladiella emersonii*

The amino acid sequence of the here investigated recombinant synthesized rhodopsin part Rh (BE) is displayed in Fig.S1.

```
        10         20         30         40         50         60
MKDKDNNLRG ACSSCNCPEY CFSPTSTLCD DCKCSVTKHP IVEQPLSRNG SFRSSGASLL

        70         80         90        100        110        120
PSPSSPNVKI TSTVGLRSRK SESQANVRGS MISNSNSGSR SNNSGGAGGG SGGSSSSKGG

       130        140        150        160        170        180
SALANYQSAM SELWSWNMML STPSLKFLTV QFTTWIVLTT VGAIYTLFFH ERQAYNRGWA

       190        200        210        220        230        240
DIWYGYGAFG FGLGLSFAYM GFTGARNPEK KALSLCLLGV NFISFMSYII IMLRLTPTIE

       250        260        270        280        290        300
GTMANPVEPA RYLEWIATCP VLILLISEIT QYPHDPYKVI VNDYALCLAG FVGAISAQQP

       310        320        330        340        350        360
WGDLAHFVSC LCFSYVVYSL WSCFTGAIDG ETQCNVEKSG LRWIRFSTIT TWSLFPITWF

       370        380        390
SYTSGLISFT VAEAGFSMID IGAKVFLTLV LVNSTV
```

**Fig.S1:** Amino acid sequence aa1-aa396 of Rh (BE). Apoprotein molar mass is $M_{apo}$ = 43.0712 kDa.

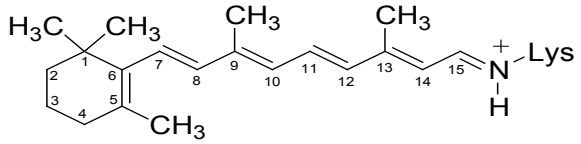

Lysine – all-*trans* protonated retinal Schiff base

$PRSB^{+}_{trans}$

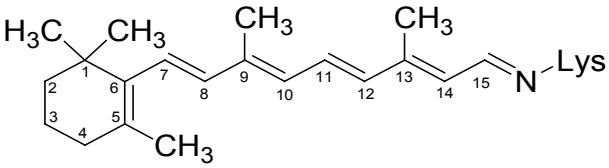

Lysine – all-*trans* retinal Schiff base

$RSB_{trans}$

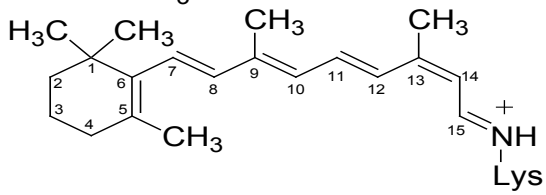

Lysine – 13-*cis* protonated retinal Schiff base

$PRSB^{+}_{cis}$

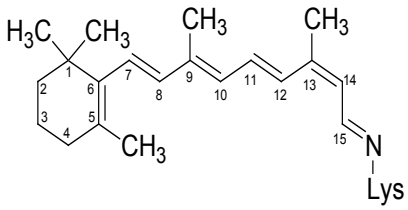

Lysine – 13-*cis* retinal Schiff base

$RSB_{cis}$

**Fig.S2:** Structural formulae of lysine coupled retinal Schiff bases.

### S2. Structural Formulae of Lysine Coupled Retinal Schiff Bases

The structural formulae of lysine coupled all-*trans* protonated retinal Schiff base, all-*trans* deprotonated retinal Schiff base, 13-*cis* protonated retinal Schiff base, and 13-*cis* deprotonated retinal Schiff base are shown in Fig.S2.

### S3. Nano-Cluster Size of Fresh Centrifuged Rh (BE)

The nano-cluster size of fresh Rh (BE) is determined analogous to the description in [77]. The scattering cross-section $\sigma_s$ is obtained from the scattering coefficient $\alpha_s$ by $\sigma_s = \alpha_s/N_{apo}$. For the sample used in Fig. 1, at λ = 632.8 nm it is $\alpha_s(\lambda)=\alpha_s(\lambda_0)(\lambda_0/\lambda)^\gamma = 0.051$ cm$^{-1}$

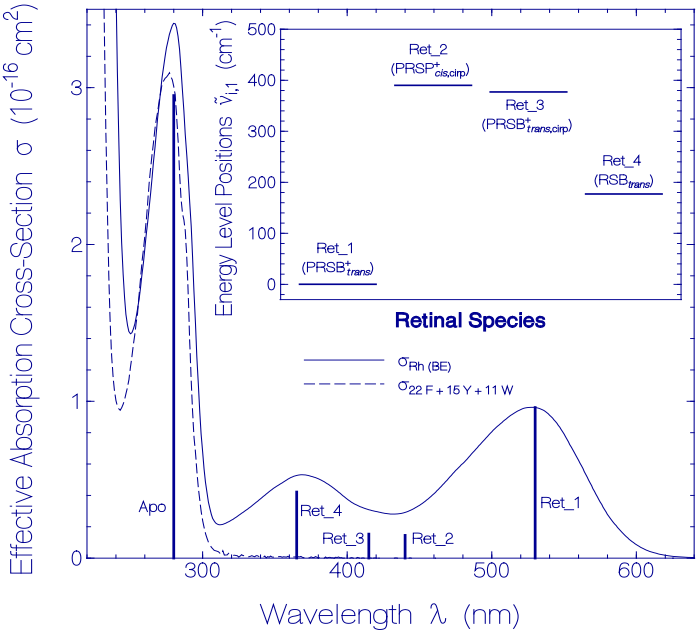


**Fig.S3:** Absorption cross-section spectra. Solid curve: effective absorption cross-section spectrum of Rh (BE). Dashed curve: expected absorption cross-section contribution $\sigma_{apo}$ of Rh (BE) apoprotein $\sigma_{apo}(\lambda) = n_{Trp}\sigma_{Trp}(\lambda) + n_{Tyr}\sigma_{Tyr}(\lambda) + n_{Phe}\sigma_{Phe}(\lambda)$ with $n_{Trp}$ = 11, $n_{Tyr}$ = 15, and $n_{Phe}$ = 22. Vertical bars: approximate absorption cross-section contributions $\sigma_i(\lambda)$ of the retinal species and the apoprotein at the selected wavelength positions of components *i*. Inset: Ground-state energy level positions in wavenumbers $\tilde{\nu}_{i,1}$ of retinal species Ret_i relative to Ret_1.

($\lambda_0$ = 800 nm, $\alpha_s(\lambda_0)$ = 0.02 cm$^{-1}$, and $\gamma$ = 4) and $\sigma_s(\lambda)$ = 2.02×10$^{-18}$ cm$^2$ ($N_{apo} = \alpha_{apo}(280\text{ nm})/\sigma_{apo}(280\text{ nm}) = \alpha_a(280\text{ nm})\,\kappa_{abs,Apo}/\sigma_{apo}(280\text{ nm}) = 2.53\times10^{16}$ cm$^{-3}$ using $\alpha_a(280\text{ nm}) = 8.74$ cm$^{-1}$, $\kappa_{abs,Apo} \approx 0.87$, $\sigma_{apo}(280\text{ nm}) = 3\times10^{-16}$ cm$^2$).

The scattering cross-section $\sigma_s$ is theoretically given by [17]

$$\sigma_s = \beta_m \tilde{M} \sigma_{R,m}, \tag{S1}$$

where $\beta_m$ is the degree of aggregation (average number of protein molecules per cluster particle), $\tilde{M}$ is the total Mie scattering function ($\tilde{M} \le 1$ decreasing with increasing aggregate size [17]), and $\sigma_{R,m}$ is the monomer Rayleigh scattering cross-section. The monomer Rayleigh scattering cross-section is given by [17]

$$\sigma_{R,m}(\lambda) = \frac{8\pi}{3}\frac{4\pi^2 n_s^4}{\lambda^4} V_m^2 \left(\frac{n_{pr}^2 - n_s^2}{n_{pr}^2 + 2n_s^2}\right)^2 = \frac{8\pi}{3}\frac{4\pi^2 n_s^4}{\lambda^4}\left(\frac{M_{pr}}{N_A \rho_{pr}}\right)^2 \left(\frac{n_{pr}^2 - n_s^2}{n_{pr}^2 + 2n_s^2}\right)^2 \tag{S2}$$

Thereby $n_s$ is the refractive index of the solvent (water buffer) at wavelength λ, $n_{pr}$ is the refractive index of the protein at wavelength λ, $V_m = M_{pr}/(N_A \rho_{pr})$ is the volume of one protein molecule, $M_{pr}$ is the molar mass of the protein monomer ($M_{pr}$ = 43071.2 g mol$^{-1}$ for Rh (BE) apoprotein), $N_A = 6.022142\times10^{23}$ mol$^{-1}$ is the Avogadro constant, and $\rho_{pr}$ is the mass density of the protein (typical value for proteins is $\rho_{pr} \approx 1.412$ g cm$^{-3}$ [78]). These numbers give a protein monomer volume of $V_m \approx 50.65$ nm$^3$ and a protein monomer radius of $a_m = [3V_m/(4\pi)]^{1/3} \approx 2.30$ nm. At λ = 632.8 nm there is $n_s$ = 1.332 and $n_{pr} \approx 1.589$ [79] giving $\sigma_{R,m}$(632.8 nm) = 2.545×10$^{-21}$ cm$^2$. Insertion into Eq.S1 gives $\beta_m \tilde{M} \approx \beta_m = \sigma_s/\sigma_{Rm} \approx 790$. The average aggregate volume is $V_{ag} = \beta_m V_m \approx 4\times10^4$ nm$^3$ and the average aggregate radius is $a_{ag} = \beta_m^{1/3} a_m \approx 21$ nm (for this size Rayleigh scattering applies and $\tilde{M} = 1$ [17]).

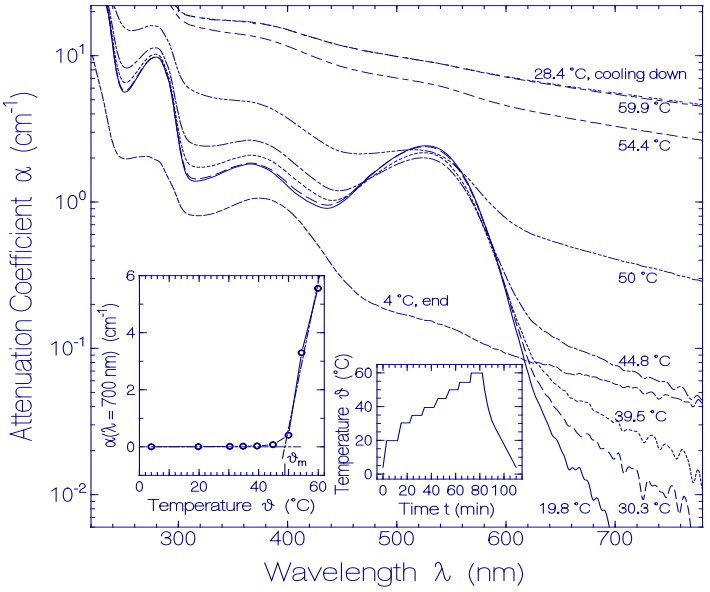


**Fig.S4a:** Heating-cooling cycle behavior of fresh dark-adapted Rh (BE) sample. Main figure: Attenuation coefficient spectra α(λ) development during stepwise sample heating up and cooling down. Right insert: Applied heating and cooling temperature profile. Left insert: Temperature dependent attenuation coefficient α(λ = 700 nm) development. The crossing point of the linearized dash-dotted curves in the low-temperature region and the high-temperature region determines the apparent protein melting temperature $\vartheta_m$ ($\vartheta_m \approx 48.8$ °C).

### S4. Approximate Absorption Cross-Section Analysis for Rh (BE)

The apparent absorption cross-section spectrum shape $\sigma_{Rh\ (BE)}(\lambda)$ of Rh (BE) (solid curve in Fig.S3) is equal to the absorption coefficient shape $\alpha_a(\lambda)$ of Fig.1. The absolute absorption cross-section spectrum $\sigma_{Rh\ (BE)}(\lambda)$ of Rh (BE) is determined by setting the absorption cross-section of Rh (BE) at λ = 280 nm equal to the apoprotein Trp, Tyr, and Phe absorption cross-section contribution $\sigma_{22F+15Y+11W}$(280 nm) and some estimated retinal absorption cross-section contribution [80]. The apoprotein absorption cross-section spectrum $\sigma_{22F+15Y+11W}$ of Rh (BE) is shown by the dashed curve in Fig.S3. It was calculated as the sum of the absorption cross-section spectra of 22 Phe, 15 Tyr, and 11 Trp residues present in one

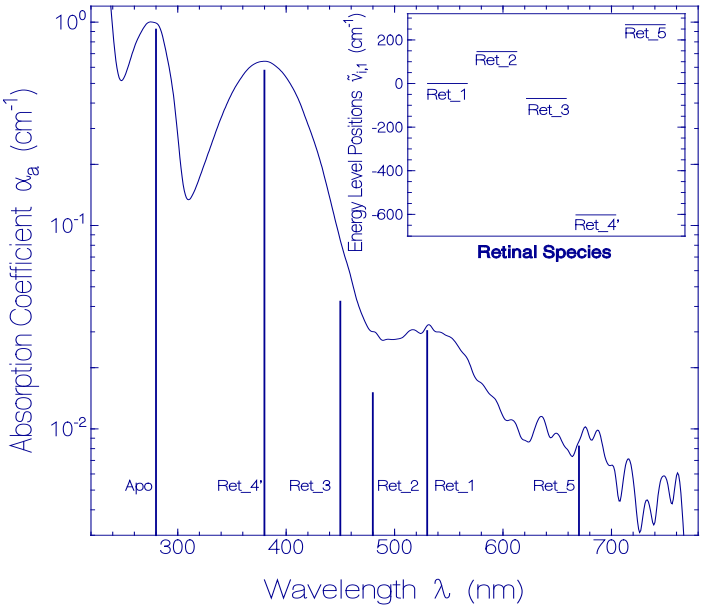


**Fig.S4b:** Absorption coefficient spectrum of heat-denatured Rh (BE) sample after centrifugation at 4 °C (4400 rpm, 15 min). Vertical bars: approximate absorption coefficients of the retinal species and the apoprotein at the selected wavelength positions. Inset: ground-state energy level positions of retinal species in heat-denatured Rh (BE).

apoprotein. The involved absorption cross-section spectra of Phe, Tyr, and Trp were taken from [29].

Fluorescence-excitation-wavelength dependent fluorescence quantum distribution measurements indicate the presence of different retinal and apoprotein species in Rh (BE) (see Fig.2). Their absorption wavelength positions and approximate absorption cross-section contributions are indicated by the bars in Fig.S3.

## S5. Protein Heat Denaturing

The thermal protein stability of Rh (BE) was studied by stepwise sample heating up to 59.9 °C, then cooling down, thereby measuring the attenuation coefficient spectra development. The apparent Rh (BE) protein melting temperature was derived from the onset of steep attenuation rise in the transparency spectral region of Rh (BE).

The applied heating-cooling temperature profile is displayed by the right inset in Fig.S4a. The main part of Fig.S4a shows attenuation coefficient spectra of Rh (BE) measured at selected temperatures during the sample heating up (start at 19.8 °C, 30.3 °C, 39.5 °C, 44.8 °C, 50 °C, 54.4 °C, 59.9 °C), cooling down (28.4 °C, cooling down, triple dotted curve), and at the end of the sample cooling down and centrifugation (4 °C, end). With rising temperature the light scattering increased. In cooling down the attenuation coefficient spectrum retained approximately unchanged (see 28.4 °C cooling down curve). Only due to centrifugation the attenuation spectrum decreased drastically (see 4 °C end curve).

The left inset in Fig.S4a shows the attenuation coefficient development at λ = 700 nm (in transparency region of Rh (BE)) with sample heating. Above 44.8 °C the measured attenuation coefficient points show a strong increase with temperature. The

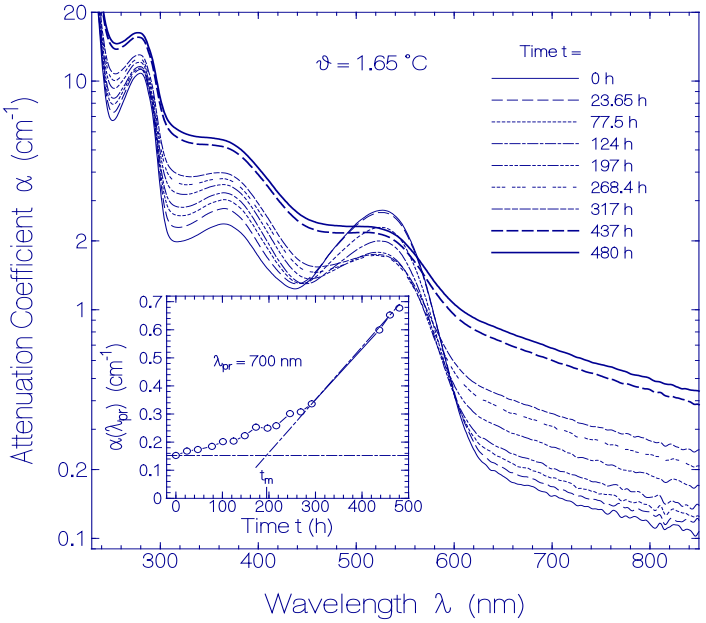


**Fig.S5:** Attenuation coefficient spectra of Rh (BE) for various sample storage times at temperature ϑ = 1.65 °C. The insert shows the temporal attenuation coefficient development at $\lambda_{pr}$ = 700 nm. The crossing point of the dash-dotted lines gives the apparent Rh (BE) protein melting time of $t_m$(1.65 °C) = 195±5 h.

**Table S1:** Spectroscopic parameters of retinals and apoprotein in a denatured Rh (BE) sample

| Parameter | Ret_1 | Ret_2 | Ret_3 | Ret_4 | Ret_5 | Apo |
|---|---|---|---|---|---|---|
| $\lambda_A$ (nm) | 530 | ≈ 480 | ≈ 450 | 380 | ≈ 670 | 280 |
| $\alpha_a(\lambda_A)$ (cm$^{-1}$) | 0.0303 | 0.0301 | 0.0845 | 0.642 | 0.0082 | 0.991 |
| $\kappa_{abs}$ | 1 | ≈ 0.5 | ≈ 0.5 | ≈ 0.9 | 1 | ≈ 0.93 |
| $\alpha_{a,Ret\_i}(\lambda_A)$ (cm$^{-1}$) | 0.0303 | ≈ 0.015 | ≈ 0.0423 | ≈ 0.578 | 0.0082 | |
| $\kappa_{Ret\_i}$ | ≈ 0.045 | ≈ 0.022 | ≈ 0.063 | ≈ 0.858 | ≈ 0.012 | |
| $\tilde{\nu}_{i,1}$ (cm$^{-1}$) | 0 | ≈ 146 | ≈ -68.7 | ≈ -602 | ≈ 270 | |

Abbreviations: $\lambda_A$: peak $S_0$-$S_1$ absorption wavelength of species *i*. $\alpha_a(\lambda_A)$: absorption coefficient at wavelength $\lambda_A$. $\kappa_{abs}$: absorption contribution of considered species *i* at $\lambda_A$. $\alpha_{a,Ret\_i}(\lambda_A)$: absorption coefficient of Ret_i at wavelength $\lambda_A$. $\kappa_{Ret,i}$: mole-fraction of retinal species *i*. $\tilde{\nu}_{i,1}$ : energy level positions of Ret_i relative to Ret_1 in wavenumbers.

onset of strong increase of light scattering with temperature is used to define an apparent melting temperature $\vartheta_m$ of the protein (the protein begins to unfold increasing its size and to cluster together to larger aggregates [22]). The crossing point of the linearized curves below the attenuation rise and above the attenuation rise is used to determine the apparent melting temperature $\vartheta_m$. A value of $\vartheta_m = 48.8\pm2$ °C is obtained.

The absorption coefficient spectrum $\alpha_a$ of Rh (BE) deprived from scattering contributions after sample cooling and centrifugation is displayed in Fig.S4b. The Rh (BE) sample absorption is strongly reduced compared to the situation before the sample heating-

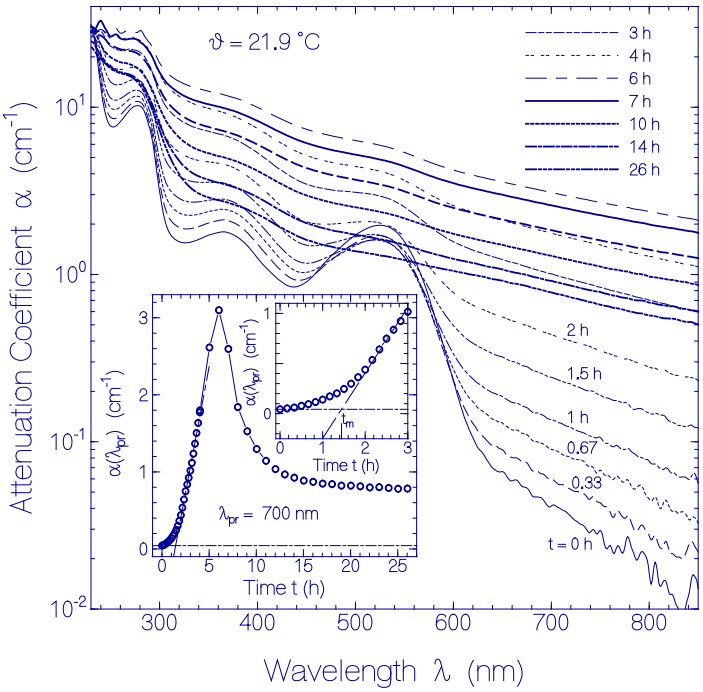


**Fig.S6:** Attenuation coefficient spectra of Rh (BE) for various sample storage times at temperature $\vartheta$ = 21.9 °C. The inset shows the temporal attenuation coefficient development at $\lambda_{pr}$ = 700 nm. The inset in the inset shows an expanded region. The crossing point of the dash-dotted lines gives the apparent Rh (BE) protein melting time $t_m$(21.9 °C) = 1.45±0.15 h.

cooling cycle. In the centrifugation process the heat-denatured protein sedimented to the bottom of the sample cell. The covalently bound retinal did not release from the rhodopsin protein in the heating process, but sedimented with the aggregated protein. The shape of the retinal spectrum in the supernatant after the heating-cooling cycle is strongly different from the shape of the retinal spectrum of fresh untreated Rh (BE). The proposed all-*trans* protonated retinal Schiff base component Ret_1 decreased strongly compared to the proposed unprotonated retinal Schiff base component Ret_4' (or Ret_4). The separation and position localization of Ret_2 and Ret_3 is aggravated by the dominant presence of deprotonated retinal Schiff base Ret_4' (Ret_4). The wavelength position of maximum absorption of the combined Ret_3 and Ret_4' (Ret_4) band changed from 368 nm before heat treatment to 380 nm after heat-denaturing indicating some change in the retinal – surrounding amino acid interaction. A small absorption band with maximum around 670 nm was resolved which is attributed to protonated 13-*cis* retinal Schiff base ($PRSB^+_{cis}$, Ret_5) absorption in denatured Rh (BE).

In Table S1 some spectroscopic parameters of the retinal species and the apoprotein are collected. The peak absorption wavelength positions $\lambda_{A,i}$ were appointed by using the absorption spectrum of Fig.S4b. The absorption coefficients $\alpha_a(\lambda_{A,i})$ are taken from Fig.S4b. The absorption contributions $\kappa_{abs,i} = \alpha_{a,i}(\lambda_{A,i})/\alpha_a(\lambda_{A,i})$ are obtained from Fig.S4b (bars and curve). The mole-fractions of species Ret_i, $\kappa_{Ret\_i}$, were calculated using Eq.3. The energy level positions were calculated using Eqs.4 and 5.

## S6. Protein Melting Time Investigations

### S6.1. Temporal Attenuation Coefficient Development at 1.65 °C

The temporal attenuation coefficient development at 1.65±0.3 °C over a time range of 480 h is displayed in Fig.S5. In the transparency region of Rh (BE) ($\lambda$ > 620 nm) the attenuation coefficient increases continuously with time indicating continued aggregate size growth

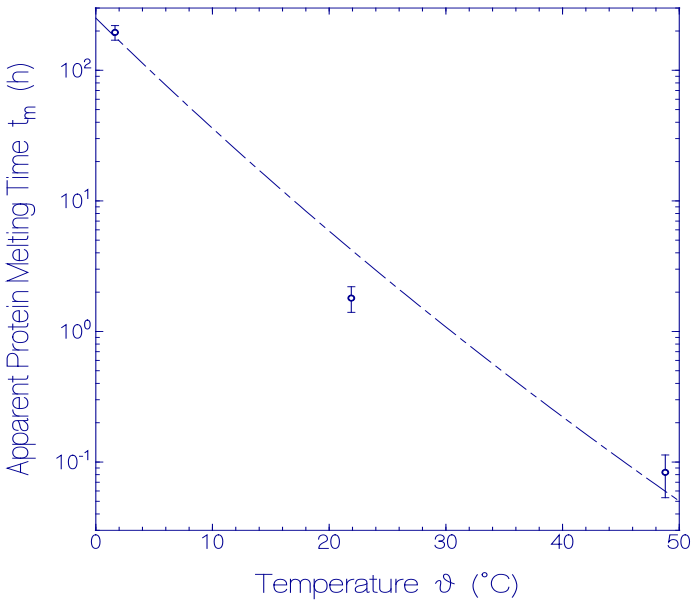


**Fig.S7:** Temporal dependence of apparent protein meting time $t_m$ of Rh (BE) in pH 8 Tris buffer. Curve is calculated using Eq.S3 with $\Delta H_{uf,i}$ = 125 kJ mol$^{-1}$ (29.9 kcal mol$^{-1}$) and $\Delta S_{uf,i}$ = 143 J K$^{-1}$ mol$^{-1}$ (34.18 cal K$^{-1}$ mol$^{-1}$).

due to the action of protein unfolding (protein melting). Only for the first absorption band around 530 nm (supposed protonated all-*trans* retinal Schiff base Ret_1) the attenuation coefficient decreased with time for the first 320 h because of thermal Ret_1 conversion to other retinal species. Then the light scattering dominated and the attenuation coefficient increased with time also in this spectral region.

The inset in Fig.S5 shows the temporal dependence of the attenuation coefficient $\alpha(\lambda_{pr})$ at $\lambda_{pr}$ = 700 nm in the transparency region of Rh (BE). For $t$ > 300 h the attenuation coefficient rises

more steeply than before indicating enhanced protein aggregation. The crossing point of the two dash-dotted lines representing the initial attenuation coefficient and the linearized attenuation coefficient above $t$ = 300 h is used to determine the apparent Rh (BE) melting time $t_m$. A value of $t_m$(1.65 °C) = 195±5 h is obtained.

**S6.2. Temporal Attenuation Coefficient Development at 21.9 °C**

The temporal attenuation coefficient development at 21.9±0.3 °C over a time range of 26 h is displayed in Fig.S6. In the transparency region of Rh (BE) (λ > 620 nm) the attenuation coefficient increased continuously with time for the first 6 h and then it decreased. It is thought that the Rh (BE) aggregate size continuously increased reaching a size where sedimentation set in and the scattering particles in the supernatant reduced. For the first absorption band around 530 nm the attenuation coefficient decreased with time for the first 1 h (Ret_1 conversion to other retinal species), then it increased with time until $t$ = 6 h due to increasing light scattering. For longer times it decreased because of aggregate sedimentation.

The main inset in Fig.S6 shows the temporal dependence of the attenuation coefficient $\alpha(\lambda_{pr})$ at $\lambda_{pr}$= 700 nm in the transparency region of Rh (BE). For $\tau < 6$ h the attenuation coefficient increased with time. For longer times $\alpha(\lambda_{pr})$= 700 nm decreased and leveled off (particle sedimentation). The inset in the inset shows an expansion of the temporal attenuation coefficient development over the first 3 h. The crossing point of the two dash-dotted lines representing the initial attenuation coefficient and the linearized attenuation coefficient above $t$ = 2 h is used to determine the apparent Rh (BE) melting time $t_m$. A value of $t_m$(21.9 °C) = 1.45±0.15 h is obtained.

**S6.3: Temperature Dependence of Apparent Rh (BE) Melting Time**

The protein melting time $t_m$ at temperature $\vartheta$ is the time interval it takes at $\vartheta$ that the protein is denatured. Here the time positions of onset of severe light scattering have been used to determine the apparent protein melting times.

In Fig.S7 the obtained apparent protein melting time $t_m$ versus sample temperature $\vartheta$ is plotted. For the protein melting time at the apparent protein melting temperature $\vartheta_m$ a time value of $t_m$= 5 min was used according to the stepwise sample heating procedure for the melting temperature determination.

The dynamics of irreversible protein unfolding was discussed in [22]. There the protein melting time was related to the Gibbs free energy of irreversible protein unfolding, $\Delta G_{uf,i}=\Delta H_{uf,i}-\vartheta\Delta S_{uf,i}$, where $\Delta H_{uf,i}$ is the enthalpy and $\Delta S_{uf,i}$ is the entropy of irreversible protein unfolding, by the following equation

$$t_m \approx \frac{h\ln(2)}{k_B\vartheta}\exp\left(\frac{\Delta G_{uf,i}}{N_A k_B\vartheta}\right)=\frac{h\ln(2)}{k_B\vartheta}\exp\left(\frac{\Delta H_{uf,i}-\vartheta\Delta S_{uf,i}}{N_A k_B\vartheta}\right) \quad \text{(S3)}$$

where $h$ is the Planck constant, $k_B$ is the Boltzmann constant, $N_A$ is the Avogadro constant, and $\vartheta$ is the temperature in Kelvin. The best fitting enthalpy and entropy values to the temperature dependence of the melting time in Fig.S7 are $\Delta H_{uf,i}$= 125 kJ mol$^{-1}$ (29.9 kcal mol$^{-1}$) and $\Delta S_{uf,i}$ = 143 J K$^{-1}$ mol$^{-1}$ (34.18 cal K$^{-1}$ mol$^{-1}$).

## References

1. Ribichich KF, Salem-Izacc SM, Georg RC, Vencio RZN, Navarro LD, et al. (2005) Gene discovery and expression profile analysis through sequencing of expressed sequence tags from different developmental stages of the chytridiomycete *Blastocladiella emersonii*. Eukaryotic Cell 4: 455-464.
2. James TY, Letcher PM, Longcore JE, Mozley-Standridge SE, Porter D, et al. (2006) A molecular phylogency of the flagellated fungi (Chytridiomycota) and description of a new phylum (Blastocladiomycota). Mycologia 98: 860-871.
3. Avelar GM, Schumacher RI, Zaini PA, Leonard G, Richards TA, et al. (2014) A rhodopsin-guanylyl cyclase gene fusion functions in visual perception in a fungus. Curr Biol 24: 1234-1240.
4. Avelar GM, Glaser T, Leonard G, Richards TA, Ulrich H, Gomes SL (2015) A cyclic GMP-dependent $K^+$ channel in the blastocladiomycete fungus *Blastocladiella emersonii*. Eukaryotic Cell 14: 958-963.
5. Silverman PM (1976) Regulation of guanylate cyclase activity during cytodiffentiation of *Blastocladiella emersonii*. Biochem Biophys Res Comm 70: 381-388.
6. Saranak J, Foster K (1987) Rhodopsin guides fungal phototaxis. Nature 387: 465-466.
7. Scheib U, Stehfest K, Gee CE, Körschen HG, Fudim R, et al. (2015) The rhodopsin-guanylyl cyclase of the aquatic fungus *Blastocladiella emersonii* enables fast optical control of cGMP signaling. Sciencesignaling 8(389): rs8.
8. Gao S, Nagpal J, Schneider MW, Kozjak-Pavlovic V, Nagel G, et al. (2015) Optogenetic manipulation of cGMP in cells and animals by the tightly light-regulated guanylyl-cyclase opsin CyclOp. Nature Comm 6: 8046 doi: 10.1038/ncomms9046.
9. Kateriya S, Nagel G, Bamberg E, Hegemann P (2004) "Vision" in single-celled algae. News Physiol Sci 19: 133-137.
10. Hegemann P (2008) Algal sensory photoreceptors. Annu Rev Plant Biol 59: 167-189.
11. Ernst OP, Lodowski DT, Elstner M, Hegemann P, Brown LS, et al. (2014) Microbial and animal rhodopsins: Structures, functions, and molecular mechanisms. Chem Rev 114: 126-163.
12. Luck M, Mathes T, Bruun S, Fudim R, Hagedorn R, et al. (2012) A photochromic histidine kinase rhodopsin (HKR1) that is bimodally switched by ultraviolet and blue light. J Biol Chem 287: 40083-40090.
13. Penzkofer A, Luck M, Mathes T, Hegemann P (2014) Bistable retinal Schiff base photodynamics of histidine kinase rhodopsin HKR1 from *Chlamydomonas reinhardtii*. Photochem Photobiol 90: 773-785.
14. Penzkofer A, Kateriya S, Hegemann P (2016) Photodynamics of the optogenetic BLUF coupled photoactivated adenylyl cyclases (PACs). Dyes and Pigments 135: 102-112.
15. Yawo H, Kandori H, Koizumi A (2015) Optogentics. Light-sensing proteins and their applications Springer Japan.
16. Kianianmomeni A (2016) Optogenetics: Methods and protocols. Methods in Molecular Biology 1408: Springer Science + Business Media New York.
17. Penzkofer A, Shirdel J, Zirak P, Breitkreuz H, Wolf E (2007) Protein aggregation studied by forward light scattering and light transmission analysis. Chem Phys 342: 55-63.

18. Förster Th (1951) Fluoreszenz organischer Verbindungen. Vandenhoeck und Ruprecht, Göttingen, Germany.

19. Holzer W, Pichlmaier M, Penzkofer A, Bradley DDC, Blau WJ (1999) Fluorescence spectroscopic behavior of neat and blended conjugated polymer thin films. Chem Phys 246: 445-462.

20. Penzkofer A (2012) Photoluminescence behavior of riboflavin and lumiflavin in liquid solutions and solid films. Chem Phys 400: 142-153.

21. Sens R (1984) Strahlungslose Desaktivierung in Xanthen-, Oxazin- und Carbazinfarbstoffen. Dissertation, Universität Gesamthochschule Siegen.

22. Penzkofer A, Stierl M, Hegemann P, Kateriya S (2011) Thermal protein unfolding in photo-activated adenylate cyclase nano-clusters from the amoeboflagellate *Naegleria gruberi* NEG-M strain. J Photochem Photobiol A: Chem 225: 42-51.

23. Vavilov SI (1927) Die Fluoreszenzausbeute von Farbstofflösungen als Funktion der Wellenlänge des anregenden Lichtes. Z Phys 42: 311-318.

24. Lewis GN, Kasha M (1944) Phosphorescence and the triplet state. J Am Chem Soc 66: 2100-2116.

25. Valeur B (2002) Molecular fluorescence. Principles and applications. Wiley-VCH Weinheim.

26. Strickler SJ, Berg RA (1962) Relationship between absorption intensity and fluorescence lifetime of molecules. J Chem Phys 37: 814-822.

27. Birks JB, Dyson DJ (1963) The relations between the fluorescence and absorption properties of organic molecules. Proc Roy Soc London Ser. A 275: 135-148.

28. Deshpande AV, Beidoun A, Penzkofer A, Wagenblast G (1990) Absorption and emission spectroscopic investigation of cyanovinyldiethylaniline dye vapors. Chem Phys 142: 123-131.

29. Lindsey JPhotochemCAD spectra by Category.

30. Turro NJ, Ramamurthy V, Scaiano JC (2009) Principles of molecular photochemistry. An introduction. University Science Books, Sausalito, California.

31. Grabowski ZR, Rotkiewicz K, Rettig W (2003) Structural changes accompanying intramolecular electron transfer: Focus on twisted intramolecular charge-transfer states and structures. Chem Rev 103: 3899-4031.

32. Chen RR (1967) Fluorescence quantum yields of tryptophan and tyrosine. Analytical Letters 1: 35-42.

33. Eisinger J, Navon G (1969) Fluorescence quenching and isotope effect in tryptophan. J Chem Phys 50: 2069-2077.

34. Kirby EP, Steiner RF (1970) The influence of solvent and temperature upon the fluorescence of indole derivatives. J Phys Chem 74: 4480-4490.

35. Bäumler W, Penzkofer A (1988) Isomerization of DODCI in the $S_0$ ground state. Chem Phys Letters 150: 315-320.

36. Voet D, Voet JG (2004) Biochemistry. 4th edition, John Wiley & Sons, Hoboken, NJ, USA: 482-505.

37. Penzkofer A (1988) Passive Q-switching and mode-locking for the generation of nanosecond to femtosecond pulses. Appl Phys B 46: 43-60.

38. Bansal AK, Penzkofer A (2008) Spectroscopic and travelling-wave lasing characterization of tetraphenylbenzidine and di-naphtalenyl-diphenylbenzidine. Appl Phys B 91: 559-569.

39. Penzkofer A, Stierl M, Mathes T, Hegemann P (2014) Absorption and emission spectroscopic characterization of photo-dymanics of photo-activated adenylyl cyclase mutant bPAC-Y7F of *Beggiatoa* sp. J Photochem Photobiol B: Biol 140: 182-193.

40. Zirak P, Penzkofer A, Lehmpfuhl C, Mathes T, Hegemann P (2007) Absorption and emission spectroscopic characterization of blue-light receptor Slr1694 from *Synechocystis* sp. PCC6803. J Photochem Photobiol B: Biol 86: 22-34.

41. Fleming GR (1986) Chemical applications of ultrafast spectroscopy. Oxford University Press, New York.

42. Kouyama T, Kinosita Jr K, Ikegami A (1985) Excited-state dynamics of bacteriorhodopsin. Biophys J 47: 43-54.

43. Kralj JM, Hochbaum DR, Douglass AD, Cohen AE (2011) Electrical spiking in *Escherchia coli* probed with a fluorescent voltage indicating protein. Science 333: 345-348.

44. Kralj JM, Douglass AD, Hochbaum DR, Maclaurin D, Cohen AE (2012) Optical recoding of action potentials in mammalian neurons using microbial rhodopsin. Nature Methods 9: 90-95.

45. Hou JH, Venkatachalam V, Cohen AE (2014) Temporal dynamics of microbial rhodopsin fluorescence reports absolute membrane voltage. Biophys J 106: 639-648.

46. Hochbaum DR, Zhao Y, Farhi SL, Klapoetke N, Werley CA, et.al. (2014) All-optical electrophysiology in mammalian neurons using engineered microbial rhodopsins. Nature Methods 11: 825-833.

47. Cohen AE (2016) Optogenetics: Turning the microscope on its head. Biophys J 110: 997-1003.

48. Nishikawa T, Murakami M, Kouyama T (2005) Crystal structure of the 13-*cis* isomer of bacteriorhodopsin in the dark-adapted state. J Mol Biol 352: 319-328.

49. Harbison GS, Smith SO, Pardoen JA, Winkel C, Lugtenburg J, et al. (1984) Dark-adapted bacteriorhodopsin contains 13-*cis*,15-*syn* and all-*trans*,15-*anti* retinal Schiff bases. PNAS 81: 1706-1709.

50. Balashov SP, Imasheva ES, Govindjee R, Ebrey TS (1996) Titration of aspargate-85 in bacteriorhodopsin: what it says about chromophore isomerization and proton release. Biophys J 70: 473-481.

51. Rupenyan A, van Stokkum IHM, Arents JC, van Grondelle R, Hellingwerf K, et al. (2008) Characterization of the primary photochemistry of proteorhodopsin with femtosecond spectroscopy. Biophys J 94: 4020-4030.

52. Kamo N, Hazemoto N, Kobatake Y, Mukohata Y (1985) Light and dark adaptation of halorhodopsin. Arch Biochem Biophys 238: 90-96.

53. Vogeley L, Sineshchekov OA, Trivedi VD, Sasahi J, Spudich JL (2004) *Anabaena* sensory rhodopsin: a photochromic color sensor at 2.0 Å. Science 306: 1390-1393.

54. Migani A, Sinicropi A, Ferré N, Cembran A, Garavelli M, et al. (2004) Structure of the intersection space accociated with Z/E photoisomerization of retinal in rhodopsin proteins. Faraday Discuss 127: 179-191.

55. Kandori H, Shichida Y, Yoshizawa T (2001) Photoizomerization in rhodopsin. Biochemistry (Moscow) 66: 1197-1209.

56. Lenz MO, Huber R, Schmidt B, Gilch P, Kalmbach R, et al. (2006) First steps of retinal photoisomerization in proteorhodopsin. Biophys J 91: 255-262.

57. Haake S, Schenkl S, Vinzani S, Chergui M (2002) Femtosecond and picoseconds fluorescence of native bacteriorhodopsin and a nonisomerizing analog. Biopolymers (Biospectroscopy) 67: 306-309.

58. Peters F, Herbst J, Tittor J, Oesterhelt D, Diller R (2009) Primary reaction dynamics of halorhodopsin, observed by sub-picosecond IR – vibrational spectroscopy. Chem Phys 323: 109-116.

59. Lutz I, Sieg A, Wegener AA, Engelhard M, Boche I, et al. (2001) Primary reactions of sensory rhodopsins. PNAS 98: 962-967.

60. Verhoefen MK, Bamann C, Blöcher R, Förster U, Bamberg E, et al. (2010) The photocycle of channelrhodopsin-2: Ultrafast reaction dynamics and subsequent reaction steps. ChemPhysChem 11: 3113-3122.

61. Wand A, Rozin R, Eliash T, Jung KH, Sheves M, et al. (2011) Asymmetric toggling of a natural photoswitch: Ultrafast spectroscopy of *Anabaena* sensory rhodopsin. J Am Chem Soc 133: 20922-20932.

62. Albani JR (2009) Fluorescence lifetimes of tryptophan: Structural origin and relation with $S_0 \rightarrow {}^1L_b$ and $S_0 \rightarrow {}^1L_a$ transitions. J Fluoresc 19: 1061-1071.

63. Oesterhelt D (1995) Structure and function of halorhodopsin. Israel J Chem 35: 475-494.

64. Béjà O, Spudich EN, Spudich JL, Leclerc M, DeLong EF (2001) Proteorhodopsin phototrophy in the sea. Nature 411: 786-789.

65. Lanyi JK (2004) Bacteriorhodopsin. Annu Rev Physiol 66: 665-688.

66.Kandori H (2015) Ion-pumping microbial rhodopsins. Frontiers in Molecular Biosciences 2: 52.

67. Inoue K, Kato Y, Kandori H (2015) Light-driven ion-translocating rhodopsins in marine bacteria. Trends in Microbiology 23: 91-98.

68. Schneider F, Grimm C, Hegemann P (2014) Biophysicis of channelrhodopsin. Annu Rev Biophys 44: 167-186.

69. Govrunova EG, Sineshchekov OA, Janz R, Liu X, Spudich JL, et al. (2015) Natural light-gated anion channels: a family of microbial rhodopsins for advanced optogenetics. Science 349: 647-650.

70. Wietek J, Prigge M (2016) Enhanced channelrhodopsins: An overview. In: A. Kianianmomeni, editor, Optogenetics: Methods and protocols. Methods in molecular biology 1408: Springer Science + Business Media New York 141-165.

71. Spudich JL (2006) The multitalented microbial sensory rhodopsins. Trends Microbiol 14: 480-487.

72. Sineshchekov OA, Trivedi VD, Sasaki J, Spudich JL (2005) Photochromicity of *Anabaena* sensory rhodopsin, an atypical microbial receptor with *cis*-retinal light-adapted form. J Biol Chem 280: 14663-14668.

73. Kawanabe A, Furutani Y, Jung K-H, Kandori H (2007) Photochromism of *Anabaena* sensory rhodopsin. J Am Chem Soc 129: 8644-8649.

74. Linder JU, Schultz JE (2003) The class III adenylyl cyclases: multi-purpose signaling modules. Cell Signal 15: 10811089.

75. Linder JU (2006) Class III adenylyl cyclases: molecular mechanisms of catalysis and regulation. Cell Mol Life Sci 63: 1736-1751.

76. Linder JU, Schultz JE (2008) Versatility of signal transduction encoded in dimeric adenylyl cyclases. Current Opinion in Structural Biology 18: 667-672.

77. Penzkofer A, Stierl M, Hegemann P, Kateriya S (2012) Absorption and fluorescence characteristics of photo-activated adenylate cyclase nano-clusters from the amoeboflagellate *Nagleria gruberi* NEG-M strain. Chem Phys 392: 46-54.

78. Fischer H, Polikarpov I, Craievich A (2004) Average protein density is a molecular-weight-dependent function. Protein Sci 13: 825-828.

79. Barer R, Tkaczyk S (1954) Refractive index of concentrated protein solutions. Nature 173: 821-822.

80. Honig B, Dinur U, Birge RR, Ebrey TG (1980) The isomer dependence of oscillator strengths in retinal and related molecules. Spectroscopic assignments. J Am Chem Soc 102: 488-494.